Karlsruhe Institute of Technology

Effects of seismic anisotropy and attenuation on first-arrival waveforms recorded at the Asse II nuclear repository

Master's Thesis of

Sonia-Adelina Șortan

at the KIT Department of Physics

Geophysical Institute (GPI)

Date of submission:

01.08.2022

Reviewer:	Prof. Dr. Thomas Bohlen
Second reviewer:	Prof. Dr. Stefan Buske
Advisor:	Dr. Thomas Hertweck
Second advisor:	Dr. Lars Houpt

Abstract

For decades, deep geological storage in former salt mines has been a widely recognized strategy for long-term radioactive waste disposal. However, in the case of the Asse II repository in Lower Saxony, groundwater inflow and instabilities in the geological structures rendered the mine unusable as a long-term solution. The nuclear waste needs to be recovered on grounds of safety reasons, hence the need for detailed structural information in order to build a new shaft. In this context, it is essential to use optimized, modern seismic imaging methods, such as, for instance, full-waveform inversion (FWI), to obtain high-resolution, physical parameter models of the Asse salt structure and its surroundings.

The goal of this thesis is to draw conclusions on the future application of elastic FWI using first-arrival waveforms at frequencies up to 20 Hz, potentially including anisotropy and attenuation. For this purpose, simple parameter models were created based on previously known geological information and used as reference for synthetic forward modeling tests. The objectives were (a) to see if the models are suitable as initial models for FWI, (b) to assess what type of anisotropy needs to be considered, if at all, and (c) to investigate the significance of attenuation. To facilitate the numerical tests, the mathematics of viscoelastic anisotropic wave propagation was studied and a new 2D finite-difference (FD) anisotropic forward solver implemented.

A detailed comparison of wavefield snapshots and seismograms was conducted between isotropic, vertical-transverse isotropic (VTI), and tilted-transverse isotropic (TTI), as well as elastic and viscoelastic modeling. The results demonstrate that, in general, the models are likely to meet the prerequisites for successful application of first-arrival FWI up to frequencies of about 20 Hz. While attenuation turned out to be only a minor factor, it is, however, essential to incorporate anisotropy. As the Asse salt structure is complex and steeply dipping, TTI modeling is the preferred way to correctly map the subsurface in high resolution and match first-arrival traveltimes. Furthermore, a comparison with field data acquired over the Asse hill shows that many features present in that data can already be explained using the current approach.

Contents

Chapter 1

Introduction

1.1 The Asse II mine

1.1.1 Regional setting

The Asse-Heeseberg structure is located in the northern foreland of the Harz Mountains, east-southeast of the Lower Saxony district of Wolfenbüttel, near Remlingen, a region that marks the transition to the North German Basin. The distinctive WNW-ESE-oriented Asse hill, with an absolute altitude of 234 meters above sea level (Remlingen Herse) and approx. eight kilometers in length and up to two kilometers in width, dominates the region (see figure 1.1). A central main valley divides the Asse-Heeseberg anticlinal structure into a southern and a northern flank, respectively, running from Groß Denkte (133 m) through the Asse I (164.5 m) and Asse II (192.5 m) shafts, to the area north-west of the Klein Vahlberger. Following a NW-SE direction, two gently-undulating continuous depressions mark the transition to sub-parts of the anticline: the basin structures of Remlingen (Remlinger Mulde) to the south and the one of Schöppenstedt (Schöppenstedter Mulde) to the north. In general, the landscape presents moderate slopes and local, steeper ruptures towards the southwest (see figure 1.2).

Figure 1.1: The Asse-Heeseberg hill (Wikipedia, 2010).

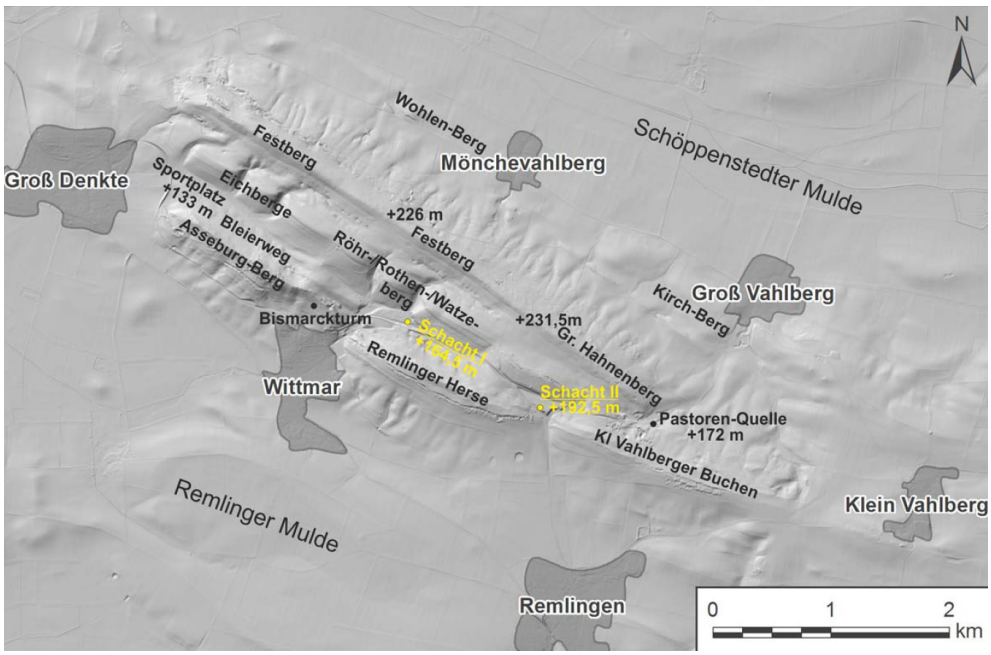

Figure 1.2: Relief structure of the Asse-Heeseberg mountain range in a LIDAR-based digital terrain model illuminated from the north-northeast. The Asse II mine is indicated in yellow (source: Bundesgesellschaft für Endlagerung, 2018).

1.1.2 Geology and tectonics

The regional geological environment corresponds to the subhercynian subsidence zone (Subhercynian Basin) upstream of the Paleozoic Harz nappe, active during Mesozoic and Cenozoic. The Asse salt formation sits atop a plateau-like structure of Zechstein base (see figure 1.3). The Asse-Heeseberg anticline formed as a result of complex tectonic processes, with the initial rise of the Zechstein salt taking place during a stretch-and-fold phase in the Jurassic, with the final formation of the anticline in the course of Cretaceous compression processes. The migration of salt from the subsoil to the NE and SW of Asse created edge depressions that absorbed thick Cretaceous deposits, which additionally drove the salt migration towards Asse due to the increased sedimentary load in these areas (Szymaniak and Schäfer, 2002). The detailed structural composition will be characterized in the following.

The Asse salt formation

The salt-structure-forming rocks present in this area, deposited periodically in the North German Basin in the Late Permian, belong to the evaporite successions from the Zechstein group: Werra, Staßfurt, Leine, Aller, Ohre, Friesland and Fulda. Most of the salt rocks at Asse originate from the Staßfurt-Formation, which predominantly consists of thick mobile rock salt. The evaporites in the Leine- and Aller-Formation have been steepened and folded during salt structure formation. The residues of the Werra-Formation as well as basal units of the Staßfurt-Formation have not been incorporated in the salt rise and remained at the Zechstein base. The top of the salt reaches from approx. −2000 m to −1800 m depth to up to −300 m depth under the Asse shafts, over a length of twenty kilometers; thus, the general tendency of the Subhercynian Basin is to dip to the west (Szymaniak and Schäfer, 2002).

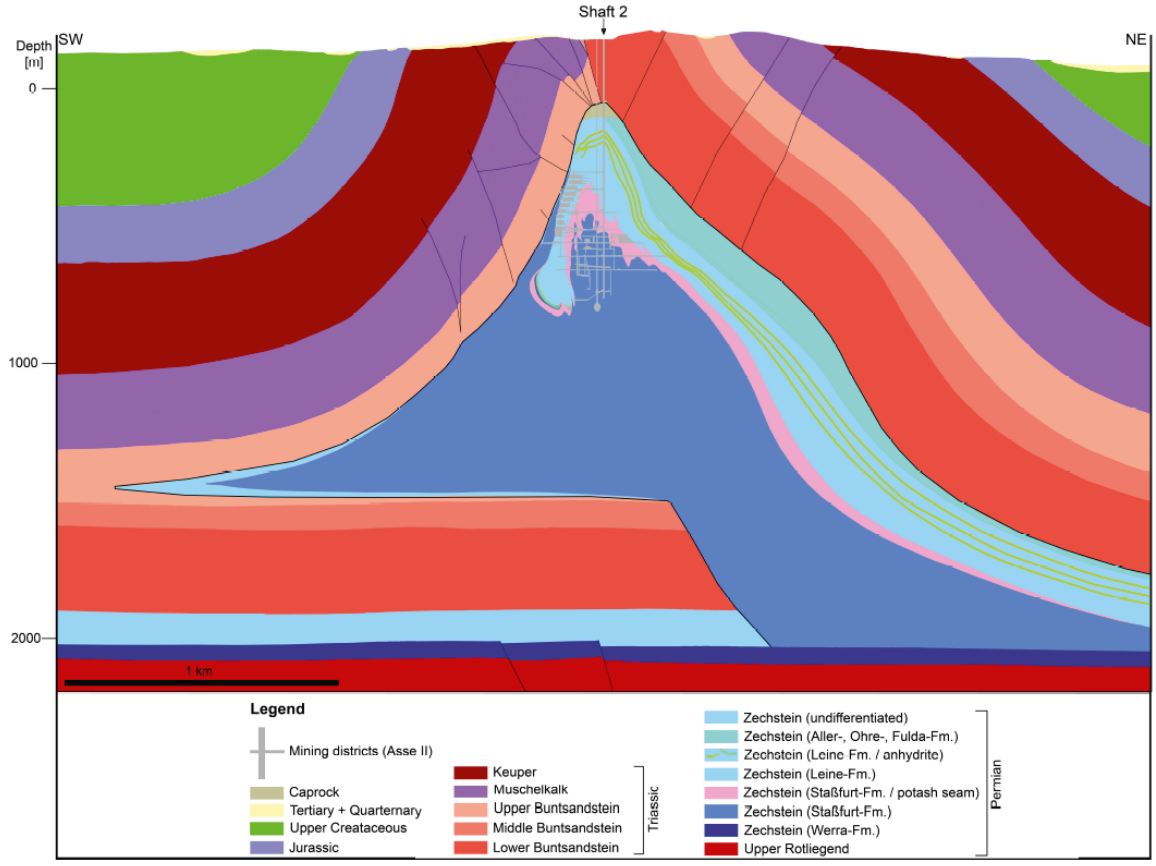

Figure 1.3: Vertical cross section of the Asse salt structure through the Asse II mine displaying the Zechstein salt formations and the sedimentary post-Permian overburden. The cross-section is oriented SW-NE, roughly perpendicular to the axis of the Asse-Heeseberg mountain range (Pollok et al., 2018).

The sedimentary overburden

During Jurassic (ca. 200 Ma), the complex outer shape and the internal composition of the Asse salt structure developed from flat, bedded salt formations to a salt pillow, when the salt rose simultaneously with the overburden. Around 140 to 85 Ma, the salt wedge was initialized, with extensional stresses building up at a 40°-direction (SW-NE), almost transversely to the Asse structure, stretching and normal-faulting the overburden stack. In the Late Cretaceous (ca. 85-65 Ma), the structure was affected by compressional tectonics. With the onset and intensification of inversion tectonics, the extensional stress field was reversed, with new compressive horizontal stresses of ca. 22° on a SSW-NNE direction; the shear planes were transformed into thrust faults and the northern flank was thrusted onto the southern one. Fracture fault zones were formed also along a SW-NE and NNW-SSE direction, with significant displacements, partially dissecting the Mesozoic overburden. However, starting about 30 Ma ago, a relaxation phase began, uplifting the entire Asse structure again and eroding it in relation to the surrounding structures. The marine transgression in Lower Oligocene further led to differential uplifts and depressions (subrosion areas) within the Asse structure as well as further uplifts compared to the basin structures of Remlingen and Schöppenstedt (see figure B.2 in the appendix) (Bundesgesellschaft für Endlagerung, 2018).

The Mesozoic overburden consists of Lower Buntsandstein (Lower Triassic), which outcrops with hard beds of oolitic and partially fossil-rich limestones. In the more steeply-sloping south-western flank of the structure, the sedimentary overburden only begins with the evaporites of the Upper Buntsandstein, which join the Zechstein ones. During the salt structure rise, the Staßfurt-Formation of the Zechstein evaporites pierced the entire Triassic overburden, of which the Middle and Lower Buntsandstein sheared off along the salt rock and, lying almost horizontally, penetrated the core of the salt structure (north-eastern flank). At the top of the central salt structure, Buntsandstein, Muschelkalk (Middle Triassic), and Keuper (Upper Triassic) are steeply asymmetrically dipping (ca. 40° to 60° at the northern flank and more than 70° at the southern flank) and strongly faulted (Bundesgesellschaft für Endlagerung, 2018).

With such a complex geological setting, the generation of a detailed subsurface model from seismic data acquired over the Asse salt structure is extremely challenging due to the complex wavefields produced by interfaces with high-impedance contrasts, and strong topography changes.

1.1.3 Salt mining and disposal

The Asse II mine is one of the four mines on the Asse-Heeseberg mountain range built at the beginning of the 20th century with the aim of extracting rock salt and potash salt. During the operational years, from 1909 to 1964, ca. five million cubic meters were dug at depths ranging from −490 m to a maximum of −775 m, leading to a total of 131 mining chambers. While the chambers used for potash salt mining at the northern flank of the Asse salt dome were back-filled right afterwards, the void volume generated after the rock salt mining (ca. 3 500 000 m^3) stayed open for decades at the southern flank.

After the mining operations ceased, the mine was bought by the German Federal Government, serving as a nuclear waste repository since then. A total of 125 787 barrels with more than 47 000 m^3 of low-level and intermediate-level radioactive waste were stored between 1967 and 1978. The thirteen former mining chambers of the mine that were chosen for emplacement have an average size of 60m × 40m × 15m and are located at three different levels (figure 1.4):

- 511-meter level: chamber no. 8a, with intermediate-low level waste (only 1.03% of the total amount of waste);
- 725-meter level: chamber no. 7, with low-level waste; the only emplacement chamber that is still accessible today, providing considerable knowledge about its condition (e.g., ceiling damage), the emplacement technology at that time and the degree of back-filling;
- 750-meter level: 11 other chambers, with low-level waste.

A research facility was also created below the 800-meter level of the former salt extraction mine in 1987, with the aim of understanding whether salt was suitable for the storage of heat-generating radioactive waste; the research work ended in 1995.

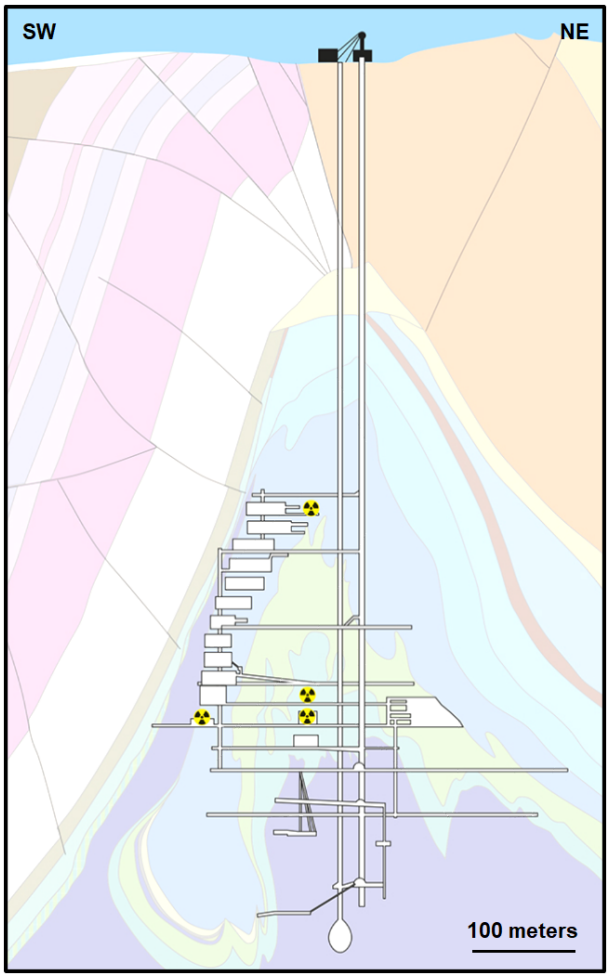

Figure 1.4: Sketch of the Asse II mine (view from southeast). The location of the nuclear waste storage chambers is marked with a radiation warning symbol (modified after Bundesgesellschaft für Endlagerung, 2021).

1.1.4 Stability problems

The mining operations at the Asse I and Asse III mines ceased decades ago due to uncontrolled water intrusion. Risks associated with the use of a salt mine as a disposal site for radioactive waste have already started to arise a few years after emplacement at the Asse II mine, too, especially at its southwestern flank. Severe deformational damage to the mine in the form of loosening of the salt rock and the rock layers and the groundwater inflow saturated with rock salt through fissures from the overlaying strata can be observed today. Most of the incoming water (around 12.5 m^3 per day) is now collected at the 658-meter level. A considerable amount of inflow water also occurs at lower levels of the mine at the southern flank, with a mean value of around 20 m^3 per day – subject to fluctuations – and with higher values of radioactive elements contamination. According to Bundesgesellschaft für Endlagerung (2022), these infiltrating solutions come mainly through areas of the Upper Buntsandstein deposits that have been loosened by mining, and enter the mine at the south-western flank . There is a risk that new inflow paths will form and radioactively contaminated salt solution could then exit the mine again via the same routes, which could cause rock pressure that would compress the mine chambers and would also allow the salt solution from the flooded mine to overflow into the surrounding rock formations, leading to possible groundwater contamination.

Another major stability problem started after some of the mining chambers were back-filled with crushed salt in the proximity of the overburden from 1995 to 2004. Although the purpose was to stabilize the mine, this only created exposure to geostatic pressure for a long time, leading to sever geomechanical damage. The chambers lie very close together, i.e., twelve meters horizontally, with six meters in between individual levels (Bundesgesellschaft für Endlagerung, 2015).

1.1.5 Retrieval plan

In 1997, the former operator of the mine presented, for the first time, a framework operating plan for the decommissioning of the Asse II mine. According to Section 9a, Paragraph 3 of the *Atomic Energy Act*, it is the task of the Federal Republic of Germany to "construct and operate a repository for radioactive waste" (Bundesgesellschaft für Endlagerung, 2022). In 2008, the Asse II mine was thus incorporated into nuclear law, meaning that decommissioning has to be prepared and implemented accordingly; starting in 2009, the *Bundesamt für Strahlenschutz* (BfS) (Federal Office for Radiation Protection) operated the mine under nuclear legislation. Various options such as a full back-filling of the chambers, waste retrieving, or internal relocation to lower depths were taken into account. With an estimated final disposal of the retrieved waste consisting of approx. 200 000 m^3, all options showed that the stipulated long-term safety could only be demonstrated by automatically retrieving the radioactive waste via a new access route that needs to be built in the direct proximity to the former emplacement chambers. Since April 2013, there has been a legal mandate for this, namely the *Act for the Acceleration of the Recovery of Radioactive Waste and the Closure of the Asse II Mine*. In April 2017, the operator responsibilities for the Asse II repository were transferred from the BfS to *Bundesgesellschaft für Endlagerung mbH* (BGE, Federal Company for Radioactive Waste Disposal), which currently plans to start the waste retrieval by no sooner than 2033.

1.2 Geophysical investigations in the area

In the context where it is not yet clear how the waste containers and storage chambers present themselves or how stable the mine itself still is anymore, the need of detailed geological information of the current salt structure is essential to facilitate a retrieval operation that is as safe as possible and also technically feasible. The current state of knowledge about the internal structure of the Asse salt body is being successively consolidated by new geophysical exploration results and incorporated in both 2D and 3D geological models.

Previous studies

On behalf of BGE, the *Bundesanstalt für Geowissenschaften und Rohstoffe* (BGR, Federal Institute for Geosciences and Natural Resources) has been actively involved since 2014 in the planning and implementation of geoscientific exploration work, allowing a coherent geological site description of the Asse salt structure (Bundesanstalt für Geowissenschaften und Rohstoffe, 2021). Different contributions to investigate the geology of the Asse salt structure for a site selection of the new, yet to be built shaft have been added (Saßnowski et al., 2018, Pollok et al.,

2018): new core drilling, borehole logging, complemented by mineralogical and geochemical analyses. The resulting information on the geological structure and external shape of the salt structure was incorporated in a 3D geological model that was supposed to be the basis for the retrieval planning. The level of detail of the model's structures varied spatially depending on the amount of available information, but was high resolution overall. The knowledge of the evaporite formations and the composition of the Asse salt structure was increased as a result of this exploration. However, BGR's results on the newly-acquired data showed quite significant differences in terms of geological assumptions compared to the previous studies, e.g., new evaporite exposures from the Leine formation, which means that the existing geological model concepts of the south-eastern part of the structure need to be revised.

Underground reflection seismics, tunnel vertical seismic profiling (VSP), and 3D borehole radar (Hupe, Orlowsky, Swoboda, et al., 2020; Hupe, Orlowsky, and Draganov, 2022) have also been applied in recent years in the salt environment of Asse, together with passive seismic interferometry (PSI). The seismic measurements resulted in mainly 2D resolution of several layer boundaries within the salt dome and also succeeded in detecting the edges of the salt dome; the borehole radar measurement provided a good 3D insight of internal stratigraphic layering, faults, and workings inside the old mining chambers. Several previously known and unknown geological structures were also identified.

Current studies

Despite more than 100 years of exploration history, the Asse salt structure is not fully understood, hence the necessity for an exact documentation, evaluation, and interpretation to obtain a better 3D geological model for resilient waste retrieval planning. As mentioned earlier, exploration results to date show a very different geology from what was expected. Therefore, a strong need to acquire new data in order to get better-resolved structural images and resolve ambiguities arose.

BfS had a preliminary study commissioned in the area in 2011 and a test measurement was carried out by *Gesellschaft für Geowissenschaftliche Dienste mbH Leipzig* (GGD) in 2013 (Bundesamt für Strahlenschutz, 2017); the test measurement has shown that the 3D-seismic procedure can be used successfully. After more than eight years of planning, BGE contracted *Geofizika Torun* to finally carry out one of the world's most dense 3D seismic measurements over the Asse structure between October 2019 and March 2020 (Bundesgesellschaft für Endlagerung, 2022). Covering a total area of 37.5 km^2, it proved to be the largest 3D live-channel-count survey ever recorded in Europe until that date. The main objectives of the 3D seismic measurements were to:

- get the best resolution of the boundaries of the salt body,
- map the fault systems,
- identify possible fluid migration paths, and
- image structures in the overburden.

1.3 Objectives of this work

Accurate seismic wave modeling of anisotropy and attenuation is essential for the understanding of wave propagation in the subsurface. Therefore, in the past decades, anisotropy of seismic velocities and attenuation have been incorporated into seismic modeling and imaging practice (e.g., Carcione et al., 1988; Komatitsch, Barnes, et al., 2000; Thomsen, 1986; Tsvankin, 2012; Bai and Tsvankin, 2016).

Because of the asymmetrical shape of the Asse salt structure, special care needs to be taken for the planning of a new shaft and infrastructure. The site selection must be done in such a way that the shaft can be constructed almost exclusively in rock salt and not in soluble potash salt. Certain safety distances to certain anhydrite rocks need to be met, together with a sufficient safety distance to the existing chambers and galleries. In the aforementioned context, with a steeply-dipping complex salt structure, rigorous finite-difference anisotropic modeling is necessary in order to have a high-resolution subsurface model in the area of the Asse salt formation. With the final ambitious aim of performing 3D viscoelastic full-waveform inversion (FWI), this study wants to first draw conclusions for future potential FWI application on first-arrival waveforms at low frequencies, i.e., up to 20 Hz. In order to do so, the two main objectives of this work are to carefully investigate the quality of the initial models to be used for FWI and to assess the influence of anisotropy and attenuation on seismic waves.

1.4 Thesis outline

This thesis is divided into six main chapters, as follows:

After the introduction, chapter 2 describes the essential theory needed to understand the methodological approach of this work. First, I derive the wave equations needed for the forward modeling; then, I present their numerical solutions using the time-domain finite-difference method.

To understand the field data, I introduce the acquisition parameters and geometry of the 3D seismic survey in chapter 3. The pre-processing steps I followed are presented there, too.

In chapter 4, the forward modeling setup is presented. First, a description of the model parameters and initial models I use to simulate observed data are presented. Then, I focus on the features of the source signature.

In chapter 5, I present the synthetic tests where I compare the results of the forward modeling for elastic isotropic, elastic anisotropic, and viscoelastic anisotropic scenarios.

In the final chapter I draw conclusions and give recommendations for further investigations.

Chapter 2

Theoretical background

In this chapter I give an overview of the most relevant concepts that are needed to solve the forward problem, i.e., to calculate the seismic wavefield given a certain distribution of model parameters. It is divided into two main sections. Section 2.1 provides an overview of the seismic wave propagation, including seismic anisotropy and attenuation. Section 2.2 focuses on the numerical implementation of the wave equations by finite differences.

2.1 Seismic wave propagation

Two equations constitute the basic principle of seismic wave propagation in arbitrary bodies: the stress-strain relation (or Hooke's law) and the equation of motion, derived from Newton's second law of motion. The necessary constitutive equations to describe wave propagation in isotropic/anisotropic and elastic/anelastic media are then derived.

Note that all equations use the Einstein notation, a convention that implies summation over repeated indices. The viscoelastic wave equations and the definitions of the material parameters are formulated in the time domain as they tend to be more efficient (though less elegant and straightforward), especially in the context of elastic and anisotropic models (Bohlen, 2002; Bai, Tsvankin, and Wu, 2017).

2.1.1 General stress-strain relation and equation of motion

The generalized Hooke's law for any elastic medium, valid for infinitesimally small deformations, is generally formulated as

$$\sigma_{ij}(t) = C_{ijkl}(t)\ \varepsilon_{kl}(t)\ , \tag{2.1}$$

where σ_{ij} represents the stress tensor, C_{ijkl} the elasticity (or stiffness) tensor, which is described in detail in subsection 2.1.3, and ε_{kl} the deformation tensor, given by

$$\varepsilon_{kl} = \frac{1}{2}\left(\frac{\partial u_k}{\partial x_l} + \frac{\partial u_l}{\partial x_k}\right)\ . \tag{2.2}$$

ε_{kl} is a second-order symmetric tensor with u_k and u_l representing the displacement of a particle in the direction of the l-th and k-th dimension, respectively, of a Cartesian coordinate system. Its derivative has the form of

$$\dot{\varepsilon}_{kl} = \frac{1}{2}\left(\frac{\partial v_k}{\partial x_l} + \frac{\partial v_l}{\partial x_k}\right) , \tag{2.3}$$

where v_k and v_l represent the l-th and k-th component, respectively, of the particle velocity. Not only ε_{kl} is a symmetric tensor, but also σ_{ij} and, consequently, C_{ijkl}.

In the special case of isotropy, the stress-strain relation in the modified form is given by

$$\sigma_{ij} = \lambda\,\theta\,\delta_{ij} + 2\,\mu\,\varepsilon_{ij} , \tag{2.4}$$

where θ denotes the cubic dilatation, i.e., the trace of ε_{ij}, and δ_{ij} is the Kronecker delta; λ and μ represent the two Lamé parameters, both of them time-invariant, with μ also referred to as the shear modulus – its combination with λ yields the P-wave modulus $\pi = \lambda + 2\mu$. By taking the derivative with respect to time, equation 2.4 becomes

$$\dot{\sigma}_{ij} = \lambda\,\frac{\partial v_k}{\partial x_k}\,\delta_{ij} + \mu\left(\frac{\partial v_i}{\partial x_j} + \frac{\partial v_j}{\partial x_i}\right) . \tag{2.5}$$

The common equation of motion in wave propagation reads

$$\rho\dot{v}_i = \frac{\partial \sigma_{ij}}{\partial x_j} + f_i \tag{2.6}$$

and states that the momentum of the medium, i.e., the actual product of density ρ and the derivative of displacement velocity, i.e., acceleration $\dot{v}_i = \frac{\partial v_i}{\partial t}$, can be changed by surface forces represented by the stress tensor σ_{ij}, or external body forces f_i. In the 2D xz-plane, an implicit representation of equation 2.6 is given by

$$\rho\dot{v}_x = \frac{\partial \sigma_{xx}}{\partial x} + \frac{\partial \sigma_{xz}}{\partial z} + f_x , \tag{2.7a}$$

$$\rho\dot{v}_z = \frac{\partial \sigma_{xz}}{\partial x} + \frac{\partial \sigma_{zz}}{\partial z} + f_z . \tag{2.7b}$$

2.1.2 Attenuation

When propagating through the Earth, the amplitudes of seismic waves decrease due to a couple of different physical phenomena: geometrical spreading, intrinsic attenuation, and scattering. Of great importance is the intrinsic (anelastic) attenuation, which represents the actual dissipation of seismic wave mechanical energy that is then converted to heat (mainly due to changes in viscosity); it is often anisotropic (Bai, 2019). To quantify its propagation effects, a dimensionless frequency-dependent parameter must be introduced, namely the seismic quality factor Q, which physically describes the relative energy loss per period: $Q(\omega) = 4\pi\,\frac{E}{\Delta E}$ (O'Connell and Budiansky, 1978).

The mathematical framework that allows us to describe the effects of attenuation is the viscoelastic model. In such a model, the stress-strain relation is governed by the presence of a time dependency referred to as the "memory (or relaxation) effect", which means that the stress σ_{ij} depends on the entire history of the strain field, not only on its current value, which is the case for purely elastic media.

$$\sigma_{ij}(t) = \dot{\Psi}_{ijkl}(t) * \varepsilon_{kl}(t) = \Psi_{ijkl}(t) * \dot{\varepsilon}_{kl}(t) \ , \tag{2.8}$$

where the star represents convolution and $\Psi_{ijkl}(t)$ is referred to as the stress-relaxation function. In order to calculate it, a mathematical model that can explain the observations must be considered. The most common method to analyze attenuation is based on mechanical (rheological) models (Knopoff and McDonald, 1958), where frequency-independent Q behavior of seismic wave propagation in the Earth's interior is approximated by a superposition of mechanical elements, i.e., a generalized standard linear solid (GSLS), introduced by Liu et al. (1976). A GSLS consists of a superposition of L rheological (Maxwell) bodies arranged in parallel, where each one provides one relaxation mechanism consisting of two other mechanical systems: a Hooke element k_0 (a single spring) for elastic behavior, and a Maxwell body (a spring k_i and a dashpot η_i in series) for absorption (Blanch et al., 1995) (see the schematic diagram in figure 2.1).

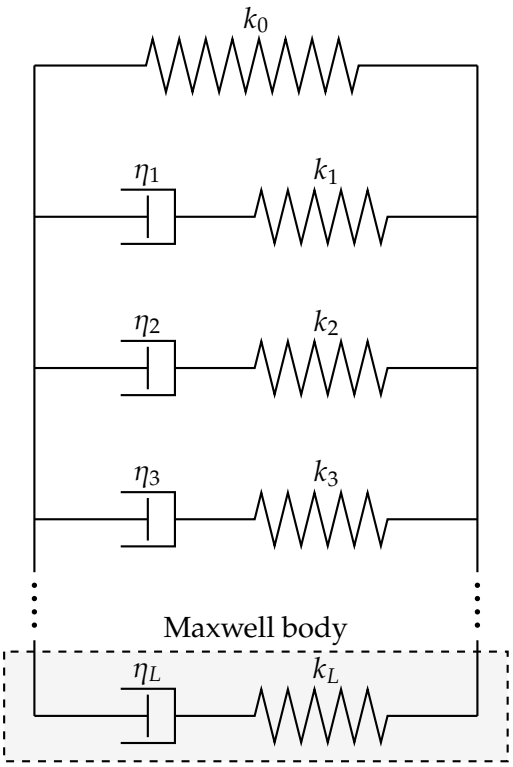

Figure 2.1: Schematic diagram of a generalized standard linear solid (GSLS) composed of L relaxation mechanisms (or Maxwell bodies), highlighted by the dashed square. k_i ($i = 1, \ldots, L$) and η_i ($i = 1, \ldots, L$) represent the elastic moduli and Newtonian viscosities, respectively, and are connected with the stress relaxation times $\tau^{\sigma l}$ and strain retardation times $\tau^{\varepsilon l}$ via $\tau^{\sigma l} = \frac{\eta_l}{k_l}$ and $\tau^{\varepsilon l} = \frac{\eta_l}{k_0} + \frac{\eta_l}{k_l}$ (after Zener, 1948; Bohlen, 2002).

With such a setup, new parameters are introduced:

- $\tau^{\sigma l}$ and $\tau^{\varepsilon l}$: stress-relaxation time and strain-retardation time, respectively, of the l-th relaxation mechanism,
- C^R: relaxed (or equilibrium) modulus , i.e., $\lim_{t\to\infty} C(t)$ (where $C(t)$ represents the stress-impulse response function of the viscoelastic medium), corresponding to the low-frequency limit, i.e., $\omega = 0$.

According to Bai and Tsvankin (2016), each relaxation process can be expressed in terms of the stress relaxation function $\Psi_{ijkl}(t)$ of the GSLS as[1]

$$\Psi_{ijkl}(t) = C^R_{ijkl} \left[1 + \sum_{l=1}^{L} \left(\frac{\tau^{\varepsilon l}_{ij}}{\tau^{\sigma l}} - 1\right) \exp\left(-\frac{t}{\tau^{\sigma l}}\right)\right] H(t) \; . \tag{2.9}$$

To simplify equation 2.9, Blanch et al. (1995) introduced the τ-method, which demonstrates that the magnitude of attenuation in anisotropic media is directly quantified by the dimensionless matrix τ_{ij}, which generally describes the attenuation parameters:

$$\tau_{ij} = \frac{\tau^{\varepsilon l}_{ij}}{\tau^{\sigma l}} - 1 \; . \tag{2.10}$$

While τ_{ij} simply vanishes in the elastic case, as $\tau^{\sigma l} = \tau^{\varepsilon l}$, it should remain constant for all L relaxation mechanisms in the viscoelastic case. Considering the τ-method, the explicit form of equation 2.9 is given by

$$\Psi_{ijkl}(t) = C^R_{ijkl} \left[1 + \sum_{l=1}^{L} \tau_{ij} \, \exp\left(-\frac{t}{\tau^{\sigma l}}\right)\right] H(t) \; . \tag{2.11}$$

Note that this relaxation function differs from the definition given in Bai and Tsvankin (2016). In the special case of isotropy, $\Psi(t)$ reads

$$\Psi_P(t) = \pi \left[1 + \sum_{l=1}^{L} \tau_P \, \exp\left(-\frac{t}{\tau^{\sigma l}}\right)\right] H(t) \tag{2.12a}$$

$$\Psi_S(t) = \mu \left[1 + \sum_{l=1}^{L} \tau_S \, \exp\left(-\frac{t}{\tau^{\sigma l}}\right)\right] H(t) \; . \tag{2.12b}$$

C_{ijkl} becomes frequency dependent due to attenuation. Bai and Tsvankin (2016) relate the relaxed modulus C^R_{ijkl}, corresponding to the model velocities, to the C_{ijkl} modulus defined at the reference frequency $\omega_0 = 2\,\pi f_0$:

$$C^R_{ijkl} = C_{ijkl}\Big|_{\omega_0} \left(1 + \sum_{l=1}^{L} \tau_{ij} \, \frac{(\omega_0 \, \tau^{\sigma l})^2}{1 + (\omega_0 \, \tau^{\sigma l})^2}\right)^{-1} \; . \tag{2.13}$$

[1]The differential calculus is firstly done in the Laplace domain and then back-transformed to the time domain.

Following Zhu and Tsvankin (2006) and equation 2.13, the mathematical matrix representation of Q is given by

$$Q_{ij}^{-1}(\omega, \tau^{\sigma l}, \tau_{ij}) = \frac{\sum_{l=1}^{L} \tau_{ij} \frac{\omega\tau^{\sigma l}}{1+(\omega\tau^{\sigma l})^2}}{1 + \sum_{l=1}^{L} \tau_{ij} \frac{(\omega\tau^{\sigma l})^2}{1+(\omega\tau^{\sigma l})^2}} \ , \tag{2.14}$$

with the substitutions $\tau = \tau_P$ and $\tau = \tau_S$, in the special case of isotropy, defining the level of attenuation for P- and S-waves, respectively. In general, the width of the frequency range in which a nearly constant Q_{ij}-spectrum can be simulated directly depends on the number of relaxation mechanisms (Bai and Tsvankin, 2016; Komatitsch and Tromp, 1999). When a GSLS consists of only one relaxation mechanism, i.e., $L = 1$, a good estimate for τ is $\tau = \frac{2}{Q}$ (Bohlen, 2002).

At $t = 0$, Ψ_{ijkl} yields the unrelaxed (or instantaneous) modulus C^U, i.e., $\lim_{t\to 0} C(t)$, which corresponds to the high-frequency limit, i.e., $\omega = \infty$.

$$C_{ijkl}^{U} \equiv \Psi_{ijkl}\Big|_{t=0} = C_{ijkl}^{R}\,(1 + L\,\tau_{ij}) \ . \tag{2.15}$$

By substituting $\Psi_{ijkl}(t)$ in the generalized stress-strain relation in viscoelastic media, and taking the time derivative on both sides, equation 2.8 becomes

$$\begin{aligned} \dot{\sigma}_{ij} &= \dot{\Psi}_{ijkl}(t) * \dot{\varepsilon}_{kl} = \\ &= C_{ijkl}^{U}\,\dot{\varepsilon}_{kl} - (C_{ijkl}^{U} - C_{ijkl}^{R}) \left[\sum_{l=1}^{L} \frac{1}{\tau^{\sigma l}} \exp\left(-\frac{t}{\tau^{\sigma l}}\right)\right] H(t) * \dot{\varepsilon}_{kl} \ . \end{aligned} \tag{2.16}$$

In order to replace the convolution terms, Carcione et al. (1988) and Robertsson et al. (1994) suggested that memory variables r_{ij}^{l} corresponding to the ij-th component for the l-th relaxation mechanism should be introduced in such a way that

$$r_{ij}^{l} = -\frac{2}{L\,\tau^{\sigma l}} (C_{ijkl}^{U} - C_{ijkl}^{R}) \exp\left(-\frac{t}{\tau^{\sigma l}}\right) H(t) * \dot{\varepsilon}_{kl} \ , \tag{2.17}$$

which becomes by differentiating with respect to time and rearranging

$$\begin{aligned} \dot{r}_{ij}^{l} = &- \frac{2}{L\,\tau^{\sigma l}} \left[-\frac{1}{\tau^{\sigma l}}(C_{ijkl}^{U} - C_{ijkl}^{R}) \exp\left(-\frac{t}{\tau^{\sigma l}}\right) H(t) * \dot{\varepsilon}_{kl}\right] - \\ &- \frac{2}{L\,\tau^{\sigma l}} (C_{ijkl}^{U} - C_{ijkl}^{R}) \exp\left(-\frac{t}{\tau^{\sigma l}}\right) \delta(t) * \dot{\varepsilon}_{kl} \ . \end{aligned} \tag{2.18}$$

Introducing the expression of r_{ij}^{l} at $t = 0$ in equation 2.18, I get

$$\dot{r}_{ij}^{l} = -\frac{2}{L\,\tau^{\sigma l}} \left[\frac{1}{2} (C_{ijkl}^{U} - C_{ijkl}^{R}) \left(\frac{\partial v_k}{\partial x_l} + \frac{\partial v_l}{\partial x_k}\right) + r_{ij}^{l}\right] \ . \tag{2.19}$$

Thus, equation 2.16 becomes

$$\dot{\sigma}_{ij} = C^{U}_{ijkl} \left(\frac{\partial v_k}{\partial x_l} + \frac{\partial v_l}{\partial x_k} \right) + \sum_{l=1}^{L} r^{l}_{ij} \ . \tag{2.20}$$

2.1.3 Seismic anisotropy and elasticity tensor

As opposed to isotropy, which means homogeneity in all directions, anisotropy is the property of directional dependency. In seismics, anisotropy describes the directional or angle dependence of the velocity of seismic waves in a medium within the Earth, which can help to characterize preferred orientation and in-situ stress conditions. If the rock properties are aligned over a greater volume extending several wavelengths, they can create certain symmetries of seismic anisotropy (Thomsen, 1986). Symmetry is a property of fundamental importance that can be studied with reference to the:

- symmetry plane – any imaginary plane passing through the center of a specific medium in such a way that it divides it in two exactly similar halves;
- symmetry axis – the imaginary line in a medium passing through its center in such a way that when the medium is given a complete rotation along this line, a certain face (taken as reference) comes to occupy the same position at least twice; the angle of rotation needs to bring a reference face to the same position, thus defining the nature of the axis of symmetry, i.e.,vertical, horizontal, tilted, etc.

The basic symmetry systems are triclinic, monoclinic, orthorhombic, and hexagonal. Hexagonal (or cylindrical) symmetry is of particular interest in seismics, as it is relatively simple but can still approximate many actual situations in the Earth, for instance where sedimentary layers are neatly ordered. The most typical anisotropic medium that exhibits hexagonal symmetry is called transversely isotropic, which means that the velocity normal to the bedding is slower than the one along it. Commonly investigated symmetries are vertical-transverse isotropy (VTI), with a vertical symmetry axis and infinite number of horizontal planes with isotropic behavior, and tilted-transverse isotropy (TTI), with a rotated symmetry axis, and thus properties changing with azimuth (Tsvankin, 2012) (see figure 2.2); the most realistic one, occurring in the case of geological structures that exhibit steep dips or severe folding, i.e., salt environments, would then be the latter. Bai and Tsvankin (2016) developed a detailed numerical demonstration and analysis of vertical-transverse isotropic attenuation by 2D time-domain finite-difference modeling, while Oh et al. (2020) developed a similar tilted-transverse version.

The structure of the stiffness tensor C_{ijkl}, previously introduced in subchapter 2.1.1, is the factor that determines the velocity and polarization of seismic waves for any propagation direction (Tsvankin, 2012), thus uniquely describing the above-mentioned symmetries and their elastic moduli. Voigt (1910) introduced a notation that allows us to reduce the number of its indices from four to two by simply transforming the indices (i, j) to m and (k, l) to n in a way that $11 \rightarrow 1$, $22 \rightarrow 2$, $33 \rightarrow 3$, $23 \rightarrow 4$, $13 \rightarrow 5$, $12 \rightarrow 6$; C_{ijkl} then becomes C_{mn}.

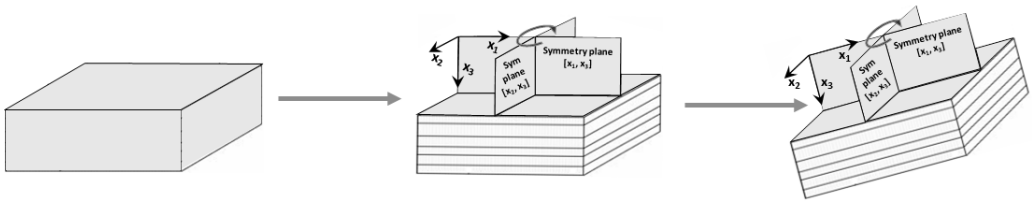

Figure 2.2: From left to right: isotropic, VTI, and TTI media in a 3D Cartesian coordinate system with $(x_1, x_2, x_3) = (x, y, z)$ (modified after TGS, 2017).

In 3D, C_{mn} is a tensor of fourth order, with $3^4 = 81$ components (however, not all of them are independent). Because of symmetry, the number of independent components is further reduced to 36:

$$\mathbf{C} = \begin{pmatrix} c_{11} & c_{12} & c_{13} & c_{14} & c_{15} & c_{16} \\ c_{12} & c_{22} & c_{23} & c_{24} & c_{25} & c_{26} \\ c_{13} & c_{23} & c_{33} & c_{34} & c_{35} & c_{36} \\ c_{14} & c_{24} & c_{34} & c_{34} & c_{45} & c_{46} \\ c_{15} & c_{25} & c_{35} & c_{45} & c_{55} & c_{56} \\ c_{16} & c_{26} & c_{36} & c_{46} & c_{56} & c_{66} \end{pmatrix}, \quad C_{mn} = C_{nm} \ . \tag{2.21}$$

As for this specific work I am assuming a polarization direction of the P-SV waves in two dimensions only, namely in the xz-plane, with the axes of the Cartesian coordinate system defined as x for crossline and z for the vertical (depth) axis, the stiffness matrix becomes a 3×3 matrix with elements defining the xx-, zz-, and xz-directions. Equation 2.21 is then reduced to

$$\mathbf{C} = \begin{pmatrix} c_{11} & c_{13} & c_{15} \\ c_{13} & c_{33} & c_{35} \\ c_{15} & c_{53} & c_{55} \end{pmatrix} . \tag{2.22}$$

In the case of isotropic media, where the elastic behavior is independent of direction, only four elastic constants are independent and they simply reduce to

$$c_{11} = c_{33} = \lambda + 2\mu = \pi \ , \tag{2.23a}$$

$$c_{13} = \lambda \ , \tag{2.23b}$$

$$c_{55} = \mu \ , \tag{2.23c}$$

which form the elements of the stiffness matrix in 2D isotropic media:

$$\mathbf{C}^{iso} = \begin{pmatrix} \pi & \lambda & 0 \\ \lambda & \pi & 0 \\ 0 & 0 & \mu \end{pmatrix} . \tag{2.24}$$

In the case of 2D VTI media, equation 2.22 reads (Thomsen, 1986)

$$\mathbf{C}^{VTI} = \begin{pmatrix} c_{11} & c_{13} & 0 \\ c_{13} & c_{33} & 0 \\ 0 & 0 & c_{55} \end{pmatrix} . \tag{2.25}$$

Under the assumption of weak anisotropy, i.e., less than 20%, these independent elastic constants have been combined by Thomsen (1986) into the so-called Thomsen anisotropic dimensionless parameters ε and δ, such that they can better describe the seismic wave propagation:

$$\varepsilon = \frac{c_{11} - c_{33}}{2c_{33}} \,, \tag{2.26a}$$

$$\delta = \frac{(c_{13} + c_{55})^2 - (c_{33} - c_{55})^2}{2c_{33}\,(c_{33} - c_{55})} \,. \tag{2.26b}$$

The vertical P- and S-wave velocities can also be expressed in terms of these elastic constants:

$$v_{P,ver} \equiv \sqrt{\frac{c_{33}}{\rho}} \quad \text{and} \quad v_{SV,ver} \equiv \sqrt{\frac{c_{55}}{\rho}} \,. \tag{2.27}$$

The angle-dependency of phase velocities, with the angle θ made by the symmetry axis of the VTI medium with the normal of the wavefront, is then given by the following approximate expressions:

$$v_P(\theta) \approx v_{P,ver}\,(1 + \delta\,\sin^2\theta\cos^2\theta + \varepsilon\,\sin^4\theta) \,, \tag{2.28a}$$

$$v_{SV}(\theta) \approx v_{SV,ver}\left(1 + \frac{v_{P,ver}^2}{v_{SV,ver}^2}\,(\varepsilon - \delta)\sin^2\theta\,\cos^2\theta\right) \,, \tag{2.28b}$$

with the maximal P-wave velocity given for a horizontal direction of wave propagation, while the maximal S-wave is reached at 45°:

$$v_{P,hor} \equiv v_{P,ver}\,(1 + \varepsilon) \,, \tag{2.29a}$$

$$v_{S,45^\circ} \equiv \frac{v_{P,hor}^2\,(\varepsilon - \delta)}{4\,v_{SV,ver}} + v_{SV,ver} \,. \tag{2.29b}$$

In the case of C_{ijkl} set along the symmetry axis, i.e., $\theta = 0°$, the elements of the stiffness matrix $\mathbf{C}^{VTI}$ in equation 2.25 can be expressed as

$$\begin{pmatrix} c_{11} \\ c_{33} \\ c_{13} \\ c_{55} \end{pmatrix} = \begin{pmatrix} \rho\,v_{P,ver}^2\,(1 + 2\,\varepsilon) \\ \rho\,v_{P,ver}^2 \\ \rho\left(\sqrt{\left(v_{P,ver}^2 - v_{SV,ver}^2\right)\left[v_{P,ver}^2\,(1 + 2\,\delta) - v_{SV,ver}^2\right]} - v_{SV,ver}^2\right) \\ \rho\,v_{SV}^2 \end{pmatrix} . \tag{2.30}$$

It can be observed that, while ε quantifies the velocity difference for wave propagation along and perpendicular to the symmetry axis, δ controls the P-wave propagation for angles near the symmetry axis.

In the case of TTI media, the stiffness matrix can be derived from the $\mathbf{C}^{VTI}$ using the Bond transformation (Bond, 1943; Carcione, 2007) as suggested by Oh et al. (2020):

$$\tilde{\mathbf{C}}^{TTI} = D(\theta_T)\,\mathbf{C}^{VTI}\,D^T(\theta_T)\,, \tag{2.31}$$

with

$$D(\theta_T) = \begin{pmatrix} \cos^2\theta_T & \sin^2\theta_T & 2\sin\theta_T\cos\theta_T \\ \sin^2\theta_T & \cos^2\theta_T & -2\sin\theta_T\cos\theta_T \\ -\sin\theta_T\cos\theta_T & \sin\theta_T\cos\theta_T & -\sin^2\theta_T \end{pmatrix}. \tag{2.32}$$

The matrix D, rotated about the vertical axis in a counter-clockwise direction, represents a simple coordinate-rotation matrix, and the parameter θ_T denotes the tilt angle of the symmetry axis measured from the vertical. With its general expression given by

$$\tilde{\mathbf{C}}^{TTI} = \begin{pmatrix} \tilde{c}_{11} & \tilde{c}_{13} & \tilde{c}_{15} \\ \tilde{c}_{13} & \tilde{c}_{33} & \tilde{c}_{35} \\ \tilde{c}_{15} & \tilde{c}_{35} & \tilde{c}_{55} \end{pmatrix}, \tag{2.33}$$

the $\tilde{c}_{ij}$ elements can be explicitly defined as

$$\begin{pmatrix} \tilde{c}_{11} \\ \tilde{c}_{33} \\ \tilde{c}_{13} \\ \tilde{c}_{55} \\ \tilde{c}_{15} \\ \tilde{c}_{35} \end{pmatrix} = \begin{pmatrix} c_{11}\cos^4\theta_T + c_{33}\sin^4\theta_T + 2\,(c_{13}+4\,c_{55})\,\sin^2\theta_T\cos^2\theta_T \\ c_{11}\sin^4\theta_T + c_{33}\cos^4\theta_T + 2\,(c_{13}+4\,c_{55})\,\sin^2\theta_T\cos^2\theta_T \\ (c_{11}+c_{33}-4\,c_{55})\,\sin^2\theta_T\cos^2\theta_T + c_{13}\,(\sin^4\theta_T+\cos^4\theta_T) \\ (c_{11}+c_{33}-2\,c_{13})\,\sin^2\theta_T\cos^2\theta_T + c_{55}\,(\cos^2\theta_T-\sin^2\theta_T)^2 \\ (c_{13}-c_{11}+2\,c_{55})\,\cos^3\theta_T\sin\theta_T - (c_{13}-c_{33}+2\,c_{55})\,\cos\theta_T\sin^3\theta_T \\ (c_{13}-c_{11}+2\,c_{55})\,\sin^3\theta_T\cos\theta_T - (c_{13}-c_{33}+2\,c_{55})\,\sin\theta_T\cos^3\theta_T \end{pmatrix}. \tag{2.34}$$

2.1.4 Anisotropic strain-stress relation in viscoelastic media

In this section, the velocity-stress formulation of the system of first-order differential equations that are the basis for the 2D FD anisotropic implementation is given. The model parameters in the implementation of viscoelastic modeling are represented by the velocities and attenuation at ω_0 and the relaxation frequencies $\tau^{\sigma l}$:

- VTI media

$$\dot{\sigma}_{xx} = c_{11}^U\,\frac{\partial v_x}{\partial x} + c_{13}^U\,\frac{\partial v_z}{\partial z} + \sum_{l=1}^{L} r_{xx}^l\,, \tag{2.35a}$$

$$\dot{\sigma}_{zz} = c_{13}^U\,\frac{\partial v_x}{\partial x} + c_{33}^U\,\frac{\partial v_z}{\partial z} + \sum_{l=1}^{L} r_{zz}^l\,, \tag{2.35b}$$

$$\dot{\sigma}_{xz} = c_{55}^U\left(\frac{\partial v_x}{\partial z} + \frac{\partial v_z}{\partial x}\right) + \sum_{l=1}^{L} r_{xz}^l\,, \tag{2.35c}$$

$$\dot{r}_{xx}^l = -\frac{1}{\tau^{\sigma l}}\left(c_{11}^R\,\tau_{11}\,\frac{\partial v_x}{\partial x} + c_{13}^R\,\tau_{13}\,\frac{\partial v_z}{\partial z} + r_{xx}^l\right)\,, \tag{2.35d}$$

$$\dot{r}_{zz}^l = -\frac{1}{\tau^{\sigma l}} \left(c_{13}^R \, \tau_{13} \, \frac{\partial v_x}{\partial x} + c_{33}^R \, \tau_{33} \, \frac{\partial v_z}{\partial z} + r_{zz}^l \right) , \tag{2.35e}$$

$$\dot{r}_{xz}^l = -\frac{1}{\tau^{\sigma l}} \left[c_{55}^R \, \tau_{55} \left(\frac{\partial v_x}{\partial z} + \frac{\partial v_z}{\partial x} \right) + r_{xz}^l \right] . \tag{2.35f}$$

- TTI media

$$\dot{\sigma}_{xx} = \tilde{c}_{11}^U \frac{\partial v_x}{\partial x} + \tilde{c}_{13}^U \frac{\partial v_z}{\partial z} + \tilde{c}_{15} \left(\frac{\partial v_x}{\partial z} + \frac{\partial v_z}{\partial x} \right) + \sum_{l=1}^{L} r_{xx}^l , \tag{2.36a}$$

$$\dot{\sigma}_{zz} = \tilde{c}_{13}^U \frac{\partial v_x}{\partial x} + \tilde{c}_{33}^U \frac{\partial v_z}{\partial z} + \tilde{c}_{35} \left(\frac{\partial v_x}{\partial z} + \frac{\partial v_z}{\partial x} \right) + \sum_{l=1}^{L} r_{zz}^l , \tag{2.36b}$$

$$\dot{\sigma}_{xz} = \tilde{c}_{15}^U \frac{\partial v_x}{\partial x} + \tilde{c}_{35}^U \frac{\partial v_z}{\partial z} + \tilde{c}_{55} \left(\frac{\partial v_x}{\partial z} + \frac{\partial v_z}{\partial x} \right) + \sum_{l=1}^{L} r_{xz}^l , \tag{2.36c}$$

$$-\tau_{\sigma l} \, \dot{r}_{xx}^l = \tilde{c}_{11}^R \, \tau_{11} \frac{\partial v_x}{\partial x} + \tilde{c}_{13}^R \, \tau_{13} \frac{\partial v_z}{\partial z} + \tilde{c}_{15}^R \, \tau_{13} \left(\frac{\partial v_x}{\partial z} + \frac{\partial v_z}{\partial x} \right) + r_{xx}^l , \tag{2.36d}$$

$$-\tau_{\sigma l} \, \dot{r}_{zz}^l = \tilde{c}_{33}^R \, \tau_{33} \frac{\partial v_z}{\partial z} + \tilde{c}_{13}^R \, \tau_{13} \frac{\partial v_x}{\partial x} + \tilde{c}_{35}^R \, \tau_{35} \left(\frac{\partial v_x}{\partial z} + \frac{\partial v_z}{\partial x} \right) + r_{zz}^l , \tag{2.36e}$$

$$-\tau_{\sigma l} \, \dot{r}_{xz}^l = \tilde{c}_{55}^R \, \tau_{55} \left(\frac{\partial v_z}{\partial x} + \frac{\partial v_x}{\partial z} \right) + \tilde{c}_{15}^R \, \tau_{15} \frac{\partial v_x}{\partial x} + \tilde{c}_{35}^R \, \tau_{35} \frac{\partial v_z}{\partial z} + r_{xz}^l . \tag{2.36f}$$

2.2 Numerical implementation by finite differences

Solving the above-mentioned wave equations analytically is only possible for very simple models. In more realistic cases, wave propagation can only be estimated using numerical approaches. One of them is the finite-differences (FD) method, in which spatial and temporal derivatives in the wave equations are approximated by FD operators, making it numerical efficient and relatively straightforward to implement. The in-house forward modeling software SOFI2D used in this work, which represents a 2D viscoelastic time domain massive parallel forward modeling code for P- and SV-waves, is based on an FD discretization (hence its abbreviation "Seismic mOdeling with FInite differences") (Bohlen et al., 2016).

2.2.1 Discretization of the wave equation

In the time-domain FD scheme, the spatial and temporal derivatives in the wave equations are approximated by FD operators, which requires the discretization of the wave equation in both space and time using a Cartesian coordinate system of equidistant grid spacing. Thus, the continuous space coordinates x and z and the time vector t are replaced by their discrete form in a way that $x = i\,\Delta h$, $z = j\,\Delta h$, and $t = n\,\Delta t$, with i, j representing the position of a specific grid point and n referring to a specific time step; Δh is the grid spacing and Δt the time sampling interval.

In this thesis, the propagation of elastic waves is modeled on a standard staggered grid (SSG) in the stress-velocity formulation, which ensures stability and high accuracy (Virieux, 1986;

Levander, 1988). On such a grid, different components of one physical parameter are defined at different staggered points. Figure 2.3 shows the locations of wavefield parameters: the two different components of the particle velocity v_i are distributed over two different staggered locations, at half grid points; the stress components σ_{ij} are distributed over two different locations: the diagonal stresses on full grid points, and the shear stresses on half grid points; the same holds for the memory variables; the material parameters, namely ρ, μ, τ, and the c_{ij} components need to be locally averaged, i.e., calculated from neighboring grid points, so that there is accuracy at strong discontinuities (Zahradnik et al., 1993; Falk, 1998; Moczo, Kristek, et al., 2002). Having the exact distribution of the viscoelastic wavefield parameters and material parameters defined, the partial derivatives using second-order FD operators (in both space and time) for any continuous function $f(x,t)$ can then be expressed as

$$\frac{\partial f}{\partial x}(n,i) = \frac{f(n,i+\frac{1}{2}) - f(n,i-\frac{1}{2})}{\Delta h} + O(\Delta h^2)\ , \tag{2.37a}$$

$$\frac{\partial f}{\partial t}(n,i) = \frac{f(n,i+\frac{1}{2}) - f(n,i-\frac{1}{2})}{\Delta t} + O(\Delta t^2)\ , \tag{2.37b}$$

for the i-th grid point and n-th time step. Following Levander (1988) and Robertsson et al. (1994), I use operators of fourth order in space and second order in time, i.e., $O(2,4)$.

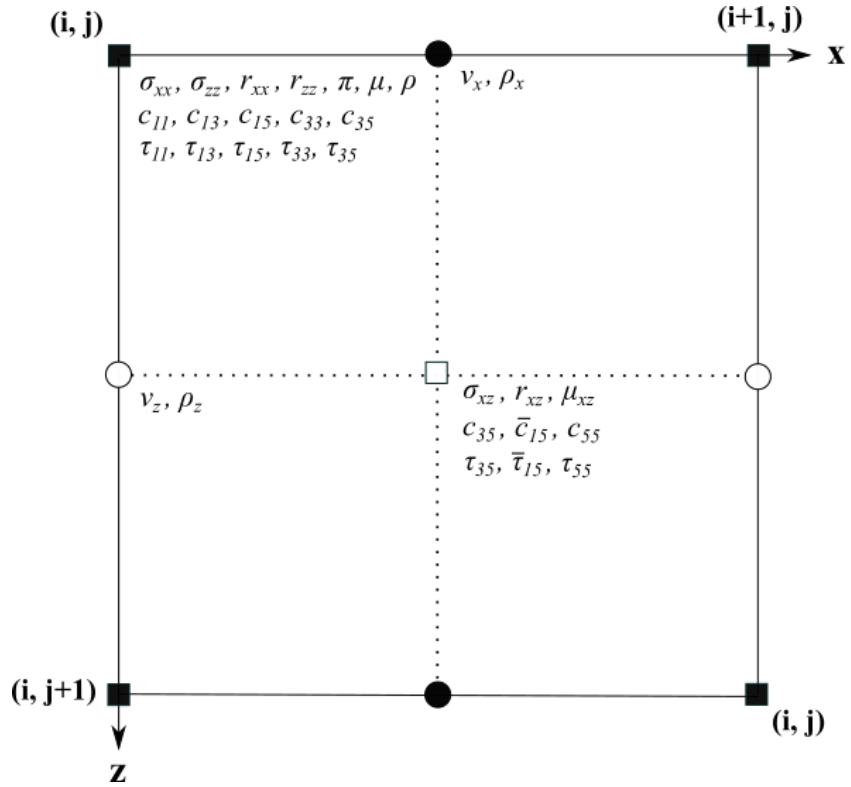

Figure 2.3: Distribution of viscoelastic anisotropic wavefield- and material parameters on an elementary finite-difference cell in the standard staggered grid (modified after Virieux, 1986). At half grid point, i.e., $(i+\frac{1}{2}, j+\frac{1}{2})$, $\bar{c}_{15}$ and $\bar{\tau}_{15}$ are harmonically- and arithmetically-averaged, respectively.

2.2.2 Initial and boundary conditions

To simulate wave propagation in a given medium, certain conditions need to be fulfilled at all times so that both stable but physically meaningful solutions of the wave equation are ensured.

Initial conditions and free surface

The interface between the (visco-)elastic medium and air at the surface plays an important role when modeling. At time $t = 0$, the medium is at rest; with no forces applied, the particle velocities, stresses, and memory variables, together with their time derivatives vanish at every spatial location (Virieux, 1986). At the top of the FD grid, a free-surface condition should be applied. However, in this study I use no explicit free surface, as the free surface is an integrated part of the model, i.e., air layer.

$$v_x\big|_{t=0} = v_z\big|_{t=0} \,, \tag{2.38a}$$

$$\sigma_{xx}\big|_{t=0} = \sigma_{zz}\big|_{t=0} = \sigma_{xz}\big|_{t=0} \,, \tag{2.38b}$$

$$r_{xx}\big|_{t=0} = r_{zz}\big|_{t=0} = r_{xz}\big|_{t=0} \,. \tag{2.38c}$$

Absorbing boundaries

In order to avoid reflections at the locations of the numerical boundaries and allow the absorption of the wavefield, I make use of perfectly matched layers (PMLs), which have proved to be a very effective way to dampen the waves near the boundaries (Komatitsch and Martin, 2007; Komatitsch and Martin, 2009). A convolutional perfectly matched layer (CPML) boundary condition is used in this case, which is achieved by a coordinate stretch of the wave equations in the frequency domain, which creates exponentially decaying plane wave solutions in the absorbing boundary frame. A width of the absorbing frame of 30 grid points was used. For the optimal realization of the PML boundary condition the dominant signal frequency occurring during the wave simulation was also specified.

2.2.3 Numerical artifacts and instability

To avoid numerical artifacts and instabilities during discretization, wavefield spatial and temporal sampling conditions have to be satisfied.

Grid dispersion

The first issue we need to address when building an FD model is finding the maximum spatial grid point distance Δh for a correct sampling of the wavefield. To avoid numerical grid dispersion, the following condition should be fulfilled at all times:

$$\Delta h \leq \frac{\lambda_{min}}{n} = \frac{v_{min}}{n\, f_{max}} \,, \tag{2.39}$$

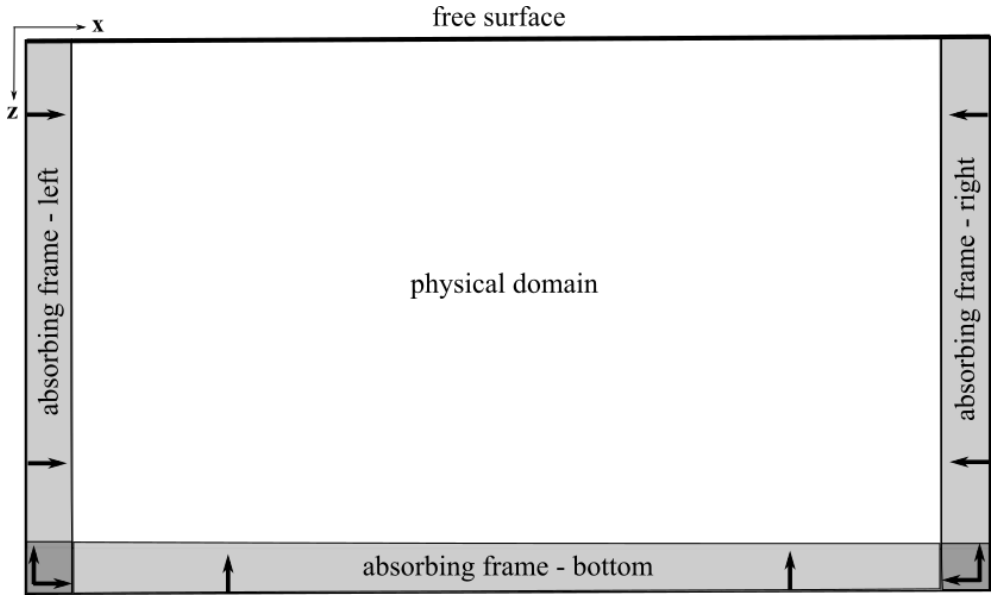

Figure 2.4: Domain boundaries in 2D. At the top of the numerical mesh a free surface boundary condition is applied; at the edges, CPML is used as an absorbing layer. The origin of the Cartesian coordinate system is at the top left corner of the grid.

where v_{min} is the minimum velocity in the model, i.e., the velocity normal to the wavefront in the case of anisotropy, n denotes the necessary number of grid points per wavelength and depends on the FD-order, e.g., $n = 8$ for a Taylor FD order of 4, which means that the spatial sampling should not surpass n points per minimum wavelength (Robertsson et al., 1994).

The Courant instability

Beside the spatial discretization, the temporal discretization also has to satisfy a sampling criterion to ensure the stability of the FD code. When a wave propagates on a discrete grid, the time step Δt has to be smaller than the time needed for the wave to travel between two adjacent grid points with grid spacing Δh (Courant-Friedrichs-Lewy criterion, Courant et al., 1928); this condition assures that in one time step the wave is not propagating further than to the adjacent grid points. Thus, the maximum value for Δt is given for a 2D grid by

$$\Delta t \leq \frac{\Delta h}{\beta \sqrt{2}\, v_{max}} \,, \tag{2.40}$$

where v_{max} is the maximum velocity in the model, i.e., not necessarily the one given for a horizontal direction of wave propagation (see equation 2.29), and β is the sum of the weighting coefficients of the FD Taylor operator and thus depends on the FD order, e.g., $\beta = 1$ for a second Taylor FD order (Courant et al., 1928).

With all the theoretical concepts for the forward problem explained, in the upcoming chapter I am going to describe the field data.

Chapter 3

Field data

In this chapter, an overview of the field data acquisition, data quality, and its pre-processing are given.

3.1 Acquisition parameters

As previously mentioned (chapter 1.2), between October 2019 and March 2020, a huge 3D seismic exploration was put in place in the area of Asse. The 37.5 km^2 survey included urban areas, crops and forests, with 93% of the originally-planned area covered in the end (Trela et al., 2021). A regular acquisition geometry with orthogonal source-receiver lines was selected (figure 3.1). In order to map the steep formations up to depths of around 2000 m, long offsets and a wide-azimuth distribution were necessary. Both source- and receiver-line spacing, i.e., distance between source and receiver lines, respectively, were reduced in the central area in order to achieve a higher resolution. A summary of the acquisition parameters is given in table 3.1.

Table 3.1: Acquisition parameters.

Source line spacing	variable (50 – 100 – 200 m)
Source point spacing	10 m
Sweep frequency range	5 – 120 Hz
Sweep length	60 s
Number of sweeps	1
Slip length	26 s
Sample rate	1 ms
Receiver line spacing	variable (50 – 100 m)
Receiver point spacing	10 m

In the agricultural and urban areas, four to five fleets of Hemi 50 vibrators were used in a slip-sweep technique, accounting for a total of 29 773 source points. Due to the rough terrain corresponding to the Asse-Heeseberg anticlinal (see figure 3.2a), in this area Vibroseis sources were replaced by dynamite, counting for ca. 18% of the total number of sources

used (6364 source points); variable shooting depths, from six to twelve meters, were used, with charges between 220 g and 1.455 kg (figure 3.2b). As this combination of Vibroseis and dynamite sources could influence the modeling and later on the FWI, this topic will be handled separately in section 3.4. Each shot was recorded by a total of 41 190 active receivers. The narrow time window for data acquisition, combined with the required fine sampling, made it necessary to use a very large active channel count, accomplished with a wireless *INOVA Quantum* nodal system consisting of 44 677 nodes (5-Hz geophones).

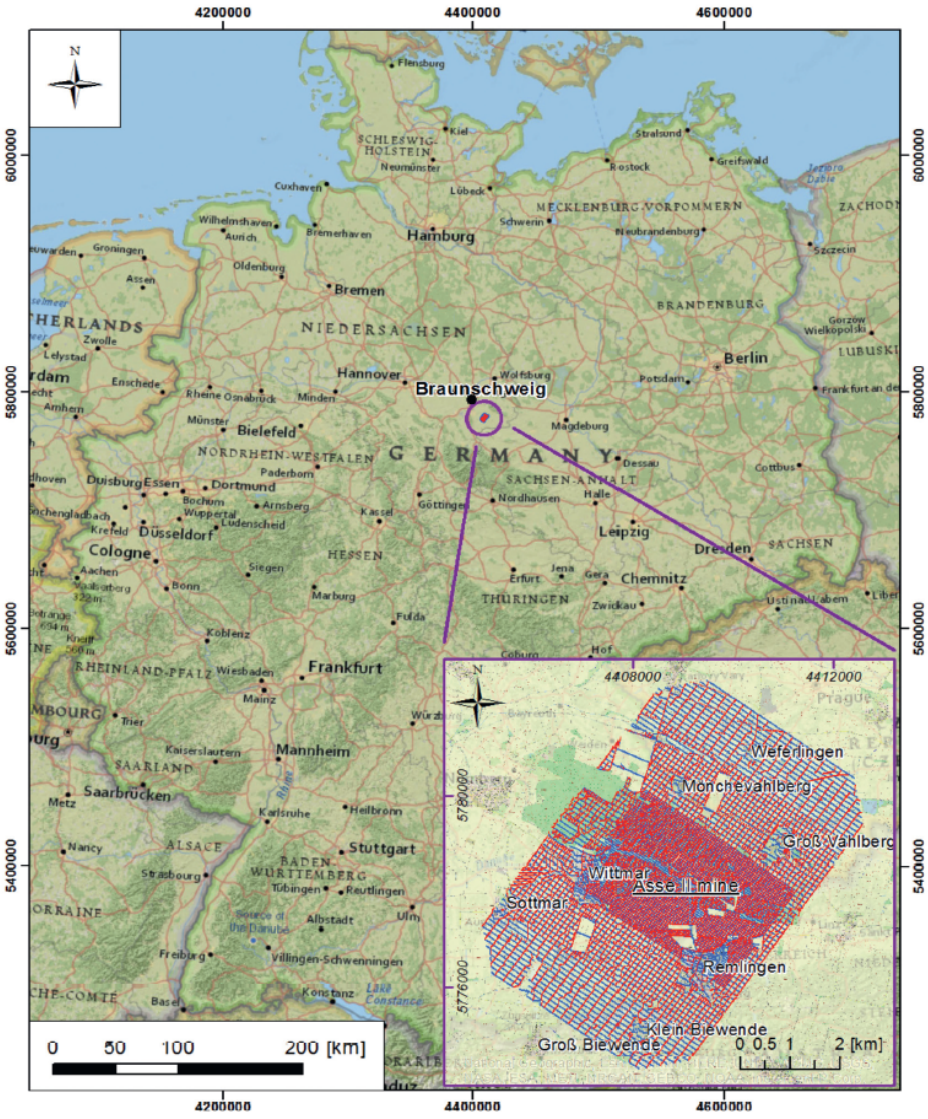

Figure 3.1: Location of the 3D seismic survey (Trela et al., 2021). A zoom-in in figure 3.5 shows the source and receiver lines, with the source lines oriented in a NW-SE direction, which corresponds not only to the strike direction of the Asse salt structure, but also to the existing grid of the roads.

The largest offset was 7680 m. Figure C.2 in the appendix depicts the fold for all offsets, i.e., the approximate number of times subsurface points are "seen" from the surface with different source-receiver distances and/or azimuths. Around 1.53 billion seismic traces were acquired, with a trace density in the central area of approx. 184 million per km^2.

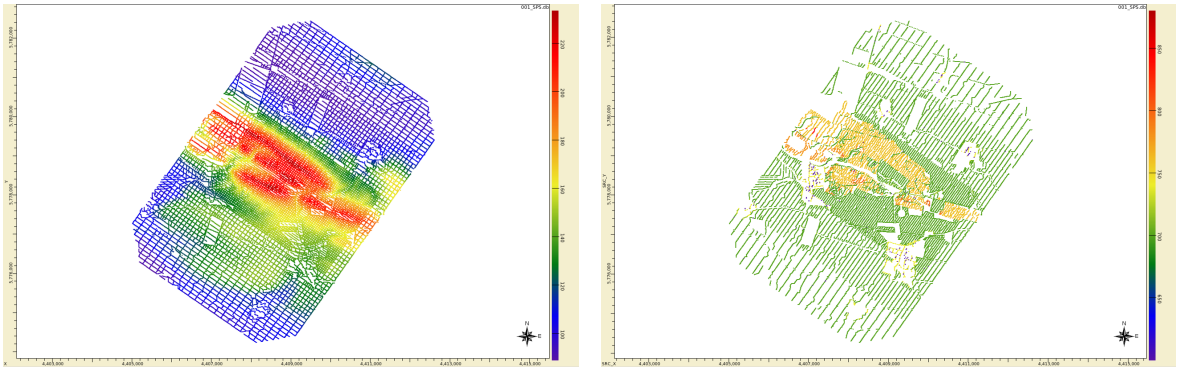

(a) Topography, ranging from 90 m to 230 m above sea level.

(b) Source types: Vibroseis in green, dynamite in yellow.

Figure 3.2: 3D seismic survey topography and types of sources.

3.2 Data quality

Figures 3.3 and 3.4 depict exemplary receiver gathers. While the Vibroseis shots have a very good data quality, with clear arrivals and no aliasing of the surface waves, the dynamite shots show a lot of scattering and few clear reflections, with significant local variation and static issues (not just elevations) caused by the rough hill area. Therefore, only Vibroseis shots will be considered for modeling in this study.

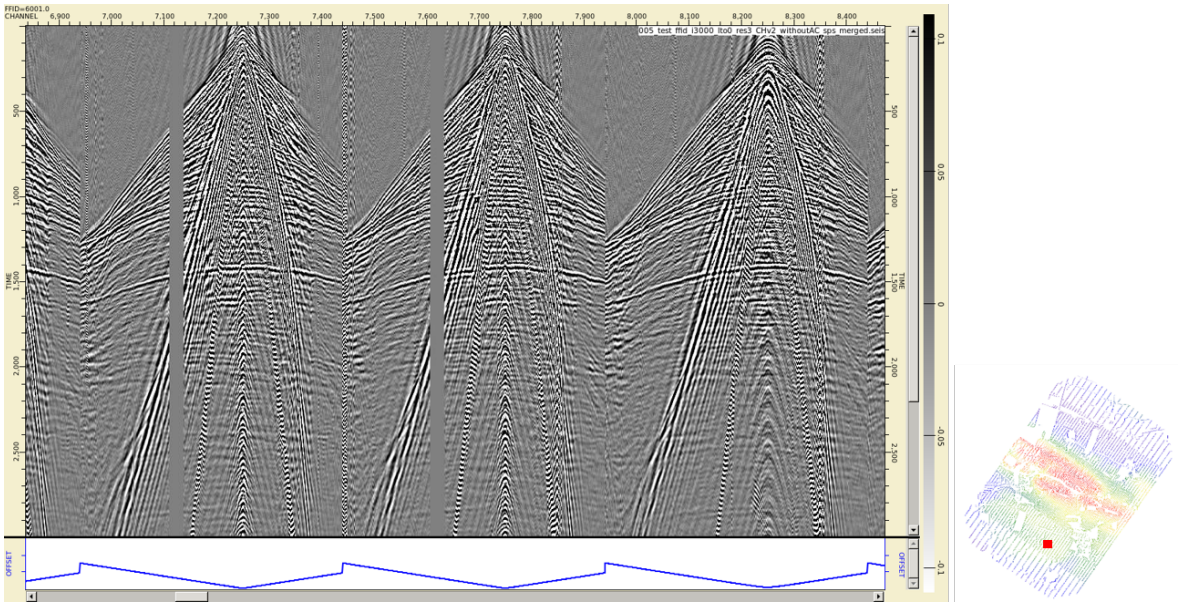

Figure 3.3: Data quality of Vibroseis shots. Three receiver gathers with the offset displayed at the bottom. To the right, the 3D topography map is shown with the exact location of the three gathers.

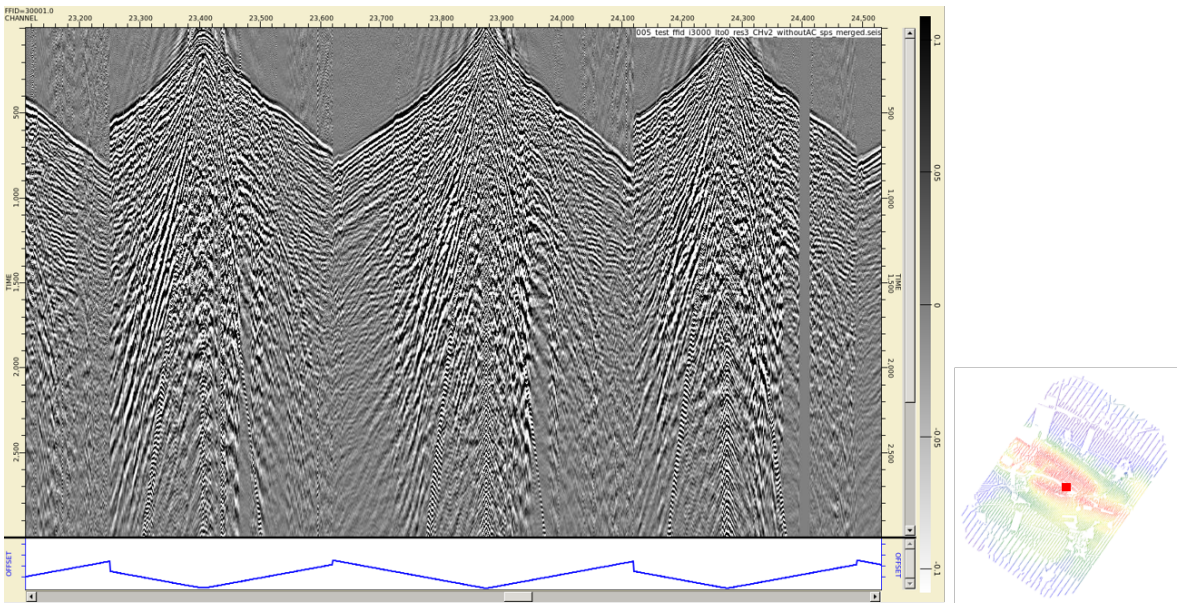

Figure 3.4: Data quality of dynamite shots. Three receiver gathers with the offset displayed at the bottom. To the right, the 3D topography map is shown with the exact location of the three gathers.

3.3 From 3D to 2D

As input, BGE delivered more than 10 Terabytes of pre-processed 3D data (correlated, with removed harmonic distortions), re-sampled to three milliseconds and minimum-phase converted, with the geometry already put up, with statics available in the headers. As for this study, a 2D line was cut from the field data for further analysis.

Based on the location of the future shaft V, the presence of existing wells and vertical-seismic profiling (VSP) R8 measurement (see figure C.1 in the appendix for more well data), and its transverse crossing over the salt body, crossline (XL) 1641 was selected (figure 3.5). Shot line 5421 and its respective receiver points were selected, aligning with XL 1641. The size of the data was significantly reduced, from orders of Terabytes to Megabytes. The number of traces was reduced from 1 529 219 940 to 66 960 traces, with 90 traces/shot.

Out of a total number of 744 shots along this crossline, 678 are Vibroseis and only 66 dynamite; the number of receivers is 101. Figure 3.6 depicts the source- and receiver-coordinate distribution along crossline 1641. It can be observed that certain sources and receivers deviate from the theoretically-straight crossline. In order to properly perform forward modeling, a 2D geometry was needed to be set up along the line so that all sources and receivers are aligned, which means that source and receiver coordinates were altered and transformed into a 2D local coordinate system, where x-axis is aligned with the direction of the crossline. The process consisted of projecting and rotating all source points onto the crossline, followed by rotating all receiver points in a way that the offset was kept constant. Figure 3.7 shows the process step by step, with all coordinates transformed from Easting-Northing into an 2D horizontal grid with $y = 0$. Horizontally, the shift between the original and altered coordinates is, in general, very small, namely below five meters; the original outliers, as expected, shifted a lot during the transformation.

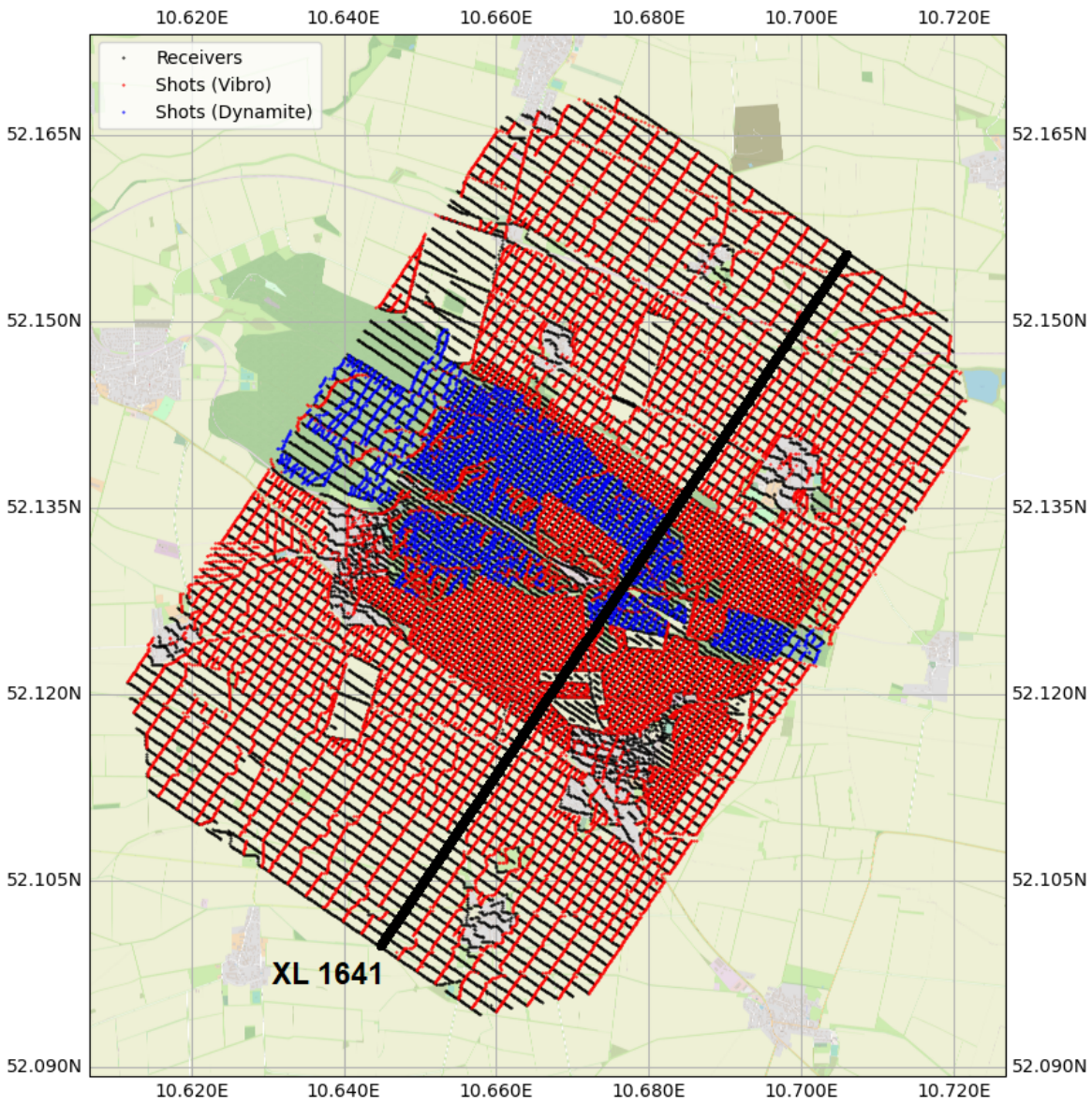

Figure 3.5: XL 1641 in the context of the 3D seismic survey. Receivers are shown in black, Vibroseis shots in red, and dynamite shots in blue.

The new elevations were assigned from an elevation table accordingly. Figure 3.8 shows the original source and receiver elevations and the altered ones after transformation. In general, the differences are in the order of 1 m to 2 m above or below the original elevations, with a few outliers in the area of the hill.

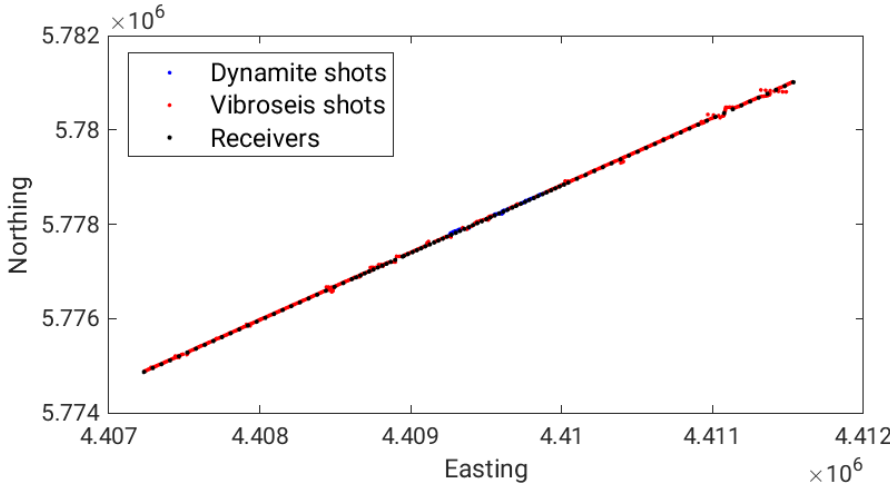

Figure 3.6: Source and receiver coordinates distribution along XL 1641. The aspect ratio is not related to the true Easting-Northing coordinates.

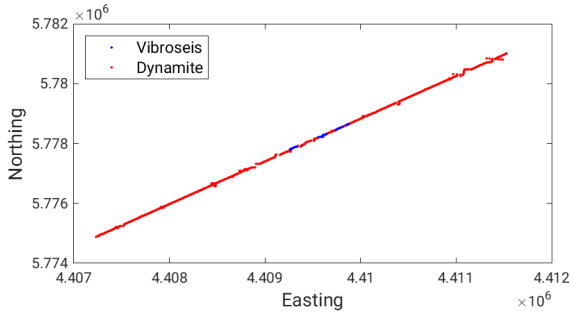

(a) Original source coordinates.

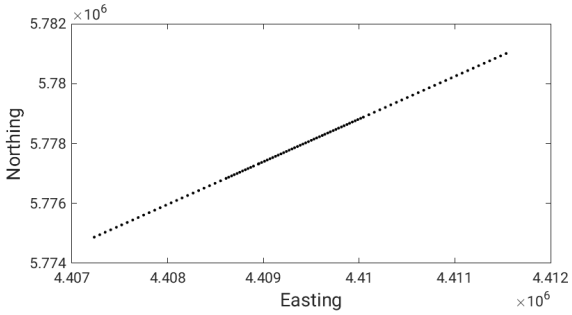

(b) Original receiver coordinates.

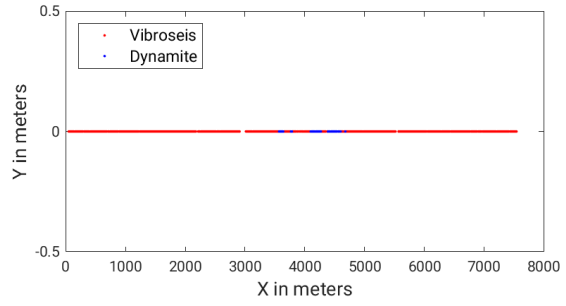

(c) Altered source coordinates.

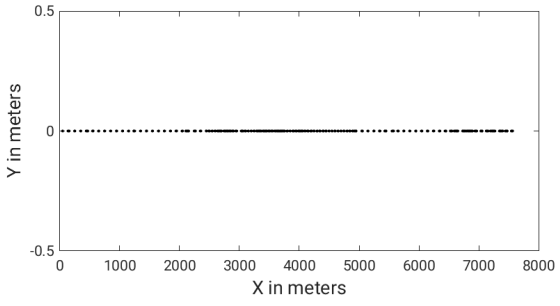

(d) Altered receiver coordinates.

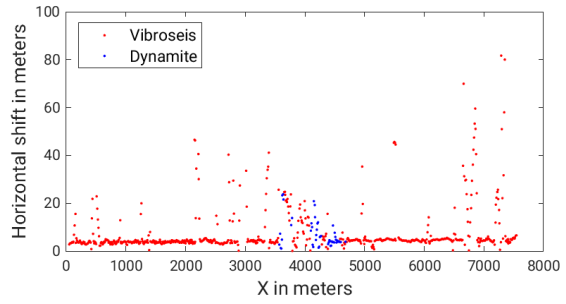

(e) Source coordinate shift.

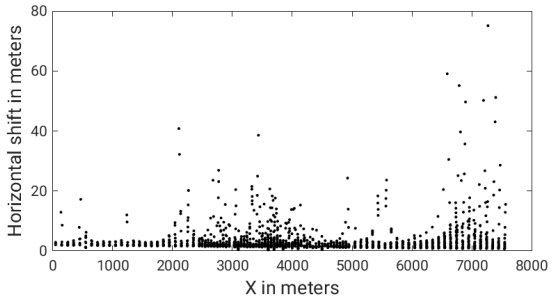

(f) Receiver coordinate shift.

Figure 3.7: Horizontal coordinate transformation along XL 1641.

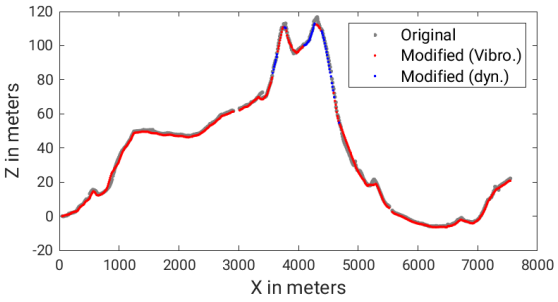

(a) Original and modified source elevations.

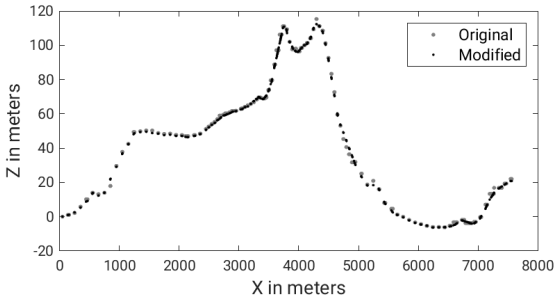

(b) Original and modified receiver elevations.

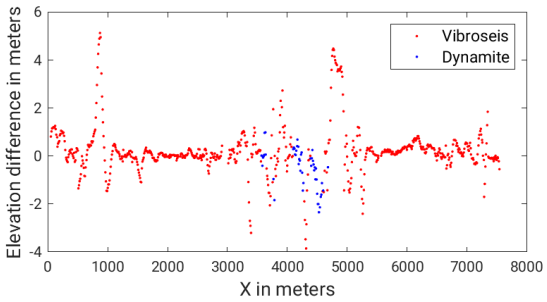

(c) Source elevation difference.

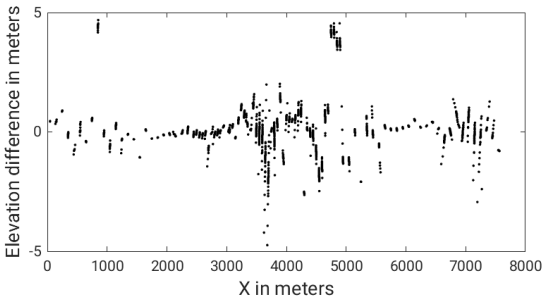

(d) Receiver elevation difference.

Figure 3.8: Vertical coordinate transformation along XL 1641 (Z-axis exaggerated).

3.4 Source signature

In the FD context, a correct source signature is needed. The final source signal used for modeling, built from the original sweep signal provided by BGE, is displayed in figure 3.9a.; as the sweep is very long, no individual cycles can be seen, therefore the start and end of the sweep is shown in figures 3.9b and 3.9c. The normalized amplitude spectra of the the sweep signal is flat for frequencies ranging between 5 Hz and 120 Hz (figure 3.9).

The autocorrelation of the sweep signature gives a Klauder wavelet, an ideal zero-phase signal, i.e., symmetrical (two-sided), with a maximum at time $t = 0$ and energy at negative times; this makes it noncausal and, therefore, not physically realizable. However, most processing is designed to deal with physical wavelets, which are causal, i.e., all values before its origin time are zero. As dynamite sources are minimum-phase, i.e., most of their signal energy resides at the start of the trace, I had to reconstruct the original minimum-phase using the minimum-phase filter that was delivered by BGE (figure 3.10). Therefore, the zero-phase Klauder wavelet depicted in figure 3.11a was convolved with the minimum-phase filter; the resulted signature is present in figure 3.11b. As I am analyzing frequencies up to 20 Hz, I applied a band-pass filter between 2 Hz with a slope of 20 dB/octave and 20 Hz with 40 dB/octave and then muted the start of the trace (figure 3.11c). In the end, in order to get the final source signature, I had to shift the wavelet by 80 ms so that it is actually minimum-phase and has most of its energy at the start of the trace; an exponential taper towards 0 was applied, too (figure 3.11d). By looking at the frequency spectra of all these wavelets (figure 3.11e), a transition from a broad frequency band of 5 Hz to 120 Hz to frequencies ranging between 5 Hz and around 20 Hz can be observed.

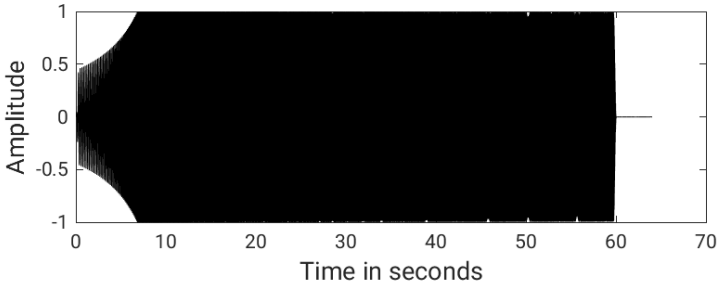

(a) Sweep signal.

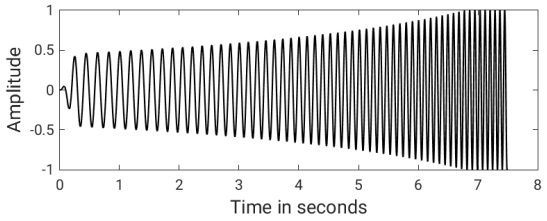

(b) Sweep start.

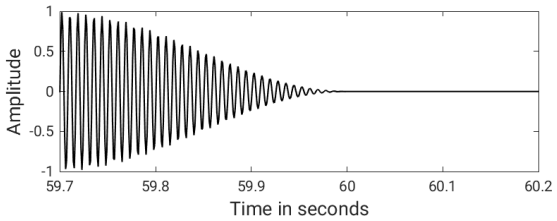

(c) Sweep end.

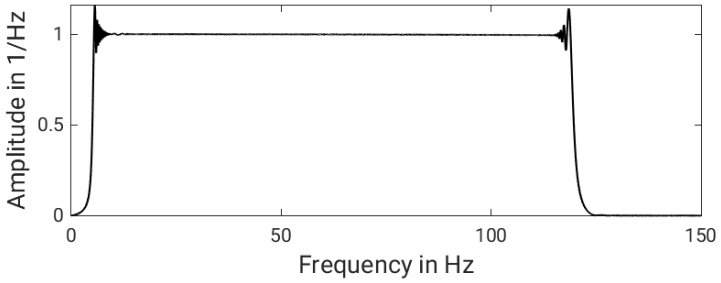

(d) Normalized amplitude spectrum.

Figure 3.9: Original sweep signature and its frequency spectrum.

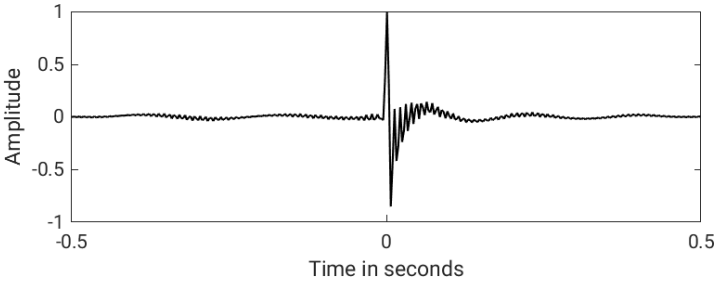

(a) Minimum-phase filter.

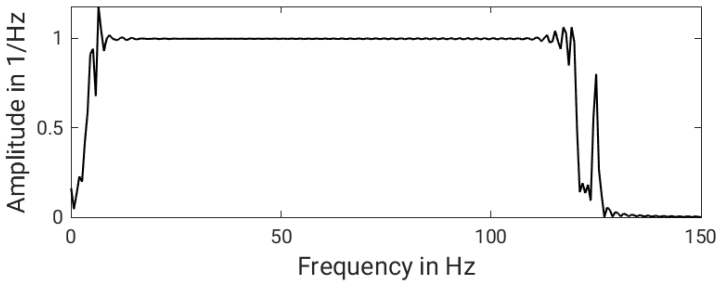

(b) Amplitude spectrum.

Figure 3.10: Minimum-phase filter and its frequency spectrum.

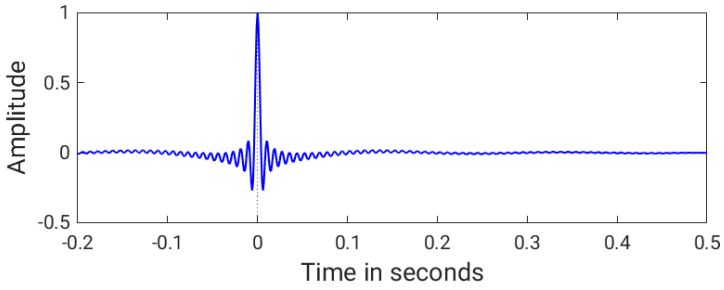

(a) Autocorrelated sweep.

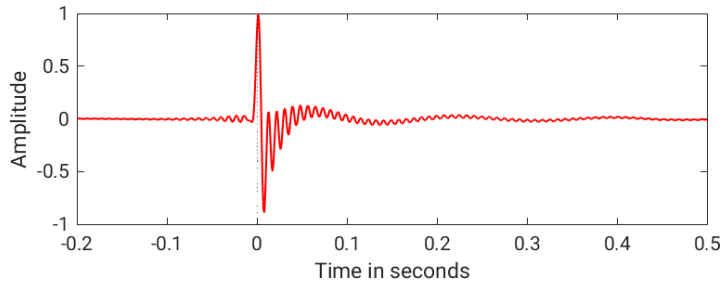

(b) Convolution of the Klauder wavelet with the minimum-phase filter.

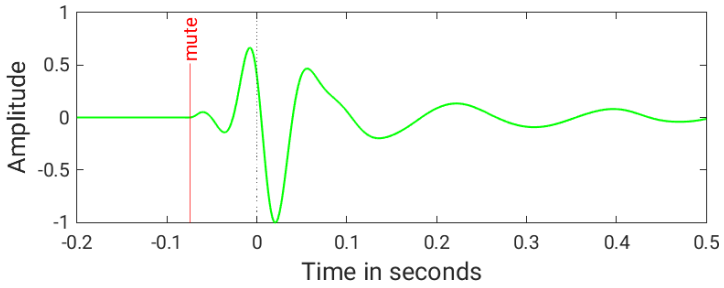

(c) Band-passed signature.

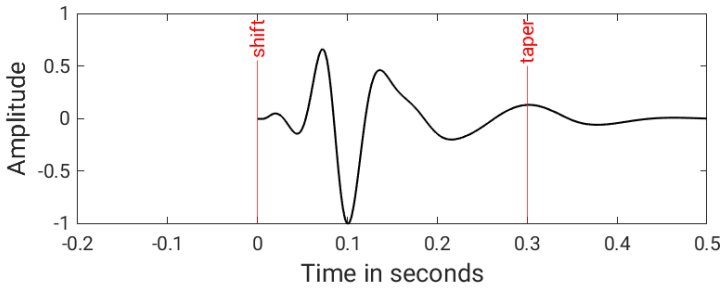

(d) Muted, shifted, and tapered signature.

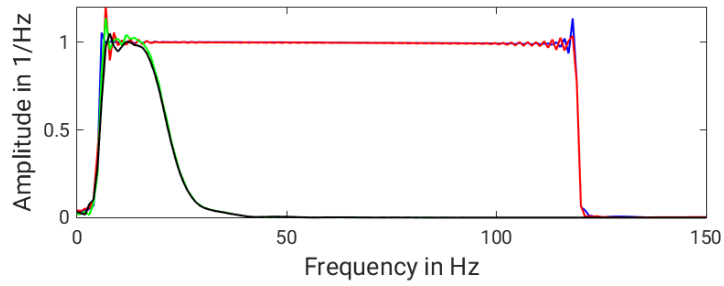

(e) Amplitude spectrum.

Figure 3.11: Signatures and their frequency spectrum.

Chapter 4

Forward modeling

For this study, the seismic forward modeling software SOFI2D based on a 2D finite-difference scheme in the time domain (e.g., Tarantola, 1984; Gauthier et al., 1986; Crase et al., 1990), originally developed by Bohlen (2002), was used, with a new and recent implementation of vertical- and tilted-transverse isotropy for both P- and SV-waves. The implementation is based on the formulas presented in chapter 2.

4.1 Model description

The models I use in my work were created based on the horizons and analytical rock-parameter relations delivered by BGE. All models are used as true models for the synthetic forward modeling tests.

4.1.1 Model parameters

In their original form, the models describe the distribution of P-wave velocity v_P, quality factor Q_P and anisotropic parameters ε and δ (Thomsen parameters) and θ (dip) – see table 4.1 below. The structure of all models is smooth, with topography on top and a general southwest-northeast orientation; the models have a depth of 3000 m and a width of 7596 m.

Table 4.1: Model-parameter distribution over the seven geological formations: (1) Cretaceous; (2) Jurassic; (3) Keuper; (4) Muschelkalk; (5) Buntsandstein; (6) Zechstein; (7) Rotliegend.

Formation	$v_{P_{min}}$ (m/s)	$v_{P_{max}}$ (m/s)	$v_{S_{min}}$ (m/s)	$v_{S_{max}}$ (m/s)	ρ_{min} (kg/m^3)	ρ_{max} (kg/m^3)	ε	δ	Q_P
1	2300	2300	1330	1330	2380	2380	0.15	0.10	140
2	2400	2400	1385	1385	2400	2400	0.15	0.10	140
3	1900	5200	1095	2000	2260	2910	0.15	0.10	120
4	2600	4500	1500	2600	2450	2810	0.15	0.10	100
5	2500	5200	1445	3000	2430	2910	0.12	0.08	80
6	4550	4550	2625	2625	2100	2100	0.00	0.00	200
7	4600	4600	2655	2655	2820	2820	0.15	0.10	80

Isotropic elastic media are described by the P-wave velocity, which is depicted in figure 4.1. Three layers, namely Keuper, Muschelkalk, and Buntsandstein, are comprised of velocity gradients; the velocity in the air was set to 0 m/s. The high-velocity contrast of the Muschelkalk layer is visible, together with the sharp interface of salt. The S-wave velocity and density were derived empirically from the P-wave velocity; the S-wave velocity is given by the ratio $\frac{v_P}{\sqrt{3}}$, while the bulk density is calculated using Gardner's relation (Gardner et al., 1974):

$$\rho = \alpha \, (k \, v_P)^{\beta} \, , \tag{4.1}$$

with constant values of $\beta = 0.25$ and $\alpha = 343$; an exception was made for salt, where a lower value of $\alpha = 256$ was assigned (as Gardner's equation is not appropriate for salt regions – Rafavich et al., 1984). Gardner's relation works without units: velocities are expressed in m/s and densities are given in kg/m^3.

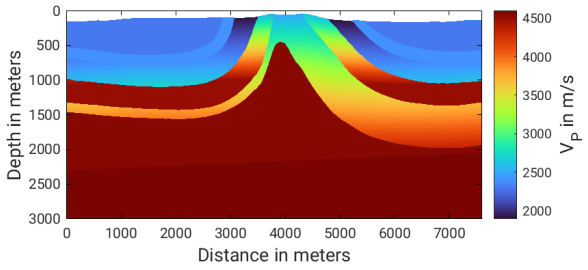

Figure 4.1: Distribution of the P-wave velocity. The S-wave velocity and density models are not shown as they are just scaled versions of the P-wave velocity model.

Anisotropic media are described by the Thomsen parameters ε and δ and the dip θ, i.e., the tilt angle of the normal of the horizons measured from the vertical in a counter-clockwise direction. The degree of anisotropy is variable, with up to 15% anisotropy (figures 4.2a and 4.2b). All formations are anisotropic, with the exception of salt, which is treated as being isotropic. The dip distribution in figure 4.2c shows the uneven steep flanks: from up to 70° to the southwest to ca. 40° to the northeast.

Viscoelastic media are described by the seismic quality factor Q, which quantifies attenuation. Figure 4.3 depicts the distribution of Q_P, which varies between 80 and 200, equivalent to rather low attenuation, with the Buntsandstein layer being the most attenuative. Q_S was set identical to Q_P; therefore, from this point onward I will refer to a general quality factor Q. As mentioned before, the frequency range in which a nearly constant Q can be simulated directly depends on the number of relaxation mechanisms. One relaxation mechanism is sufficient for my low-frequency modeling, as I get an almost flat Q-approximation response for frequencies between 6 Hz and 20 Hz.

4.1.2 Model setup

The initial dimensions of the model, as previously-stated, are 7596 m × 3000 m. Boundary zones of 30 grid points were added to all sides of the model so that any reflections of the model boundary are avoided; with an original grid size of 1 m × 1 m, this led to final model dimensions of 7656 m × 3030 m (or 7656 × 3030 grid points).

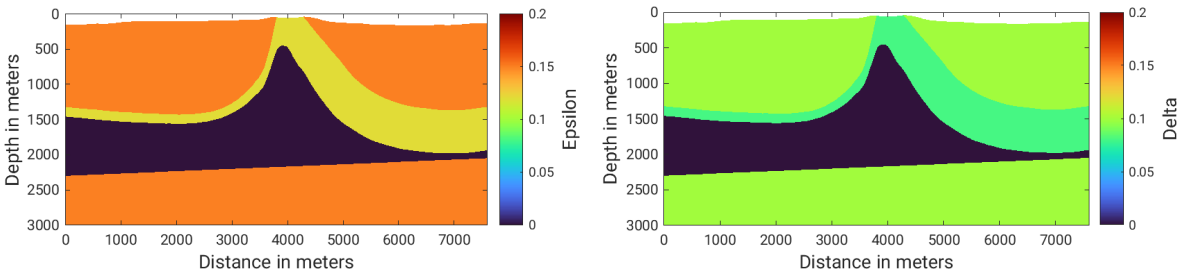

(a) Epsilon. **(b)** Delta.

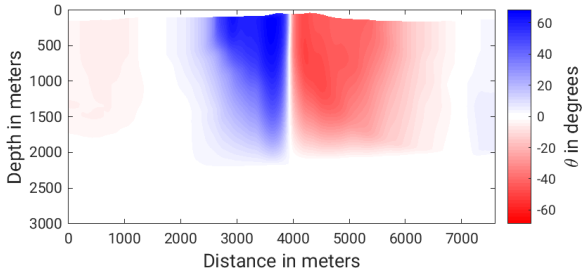

(c) Dip.

Figure 4.2: Distribution of the anisotropic model parameters.

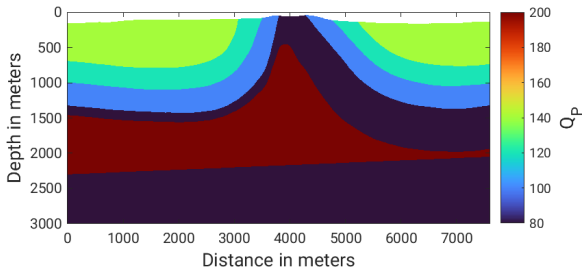

Figure 4.3: Distribution of the viscoelastic model parameters: Q_P.

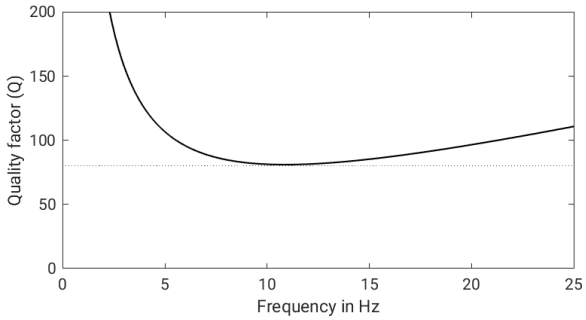

Figure 4.4: Q approximation for $L = 1$, with an almost flat response between 6 Hz and 20 Hz.

Varying topography in FD modeling can only be represented by staircases (figure 2.3). As the true topography in the area shows strong variations, with height differences of up to 140 m, I had to carefully handle the topography on the standard staggered grid. Following the distribution of physical parameters in an SSG cell, with the vertical component of the particle velocity calculated at half grid points, I positioned all vertical point sources and receivers at half grid points, too, so that any numerical issues are avoided during modeling (figure 4.5). For this reason, small changes of less than 1 m appear between elevations in the modeling and elevations in the field data; given that these changes are much smaller than the dominant wavelength, they were ignored.

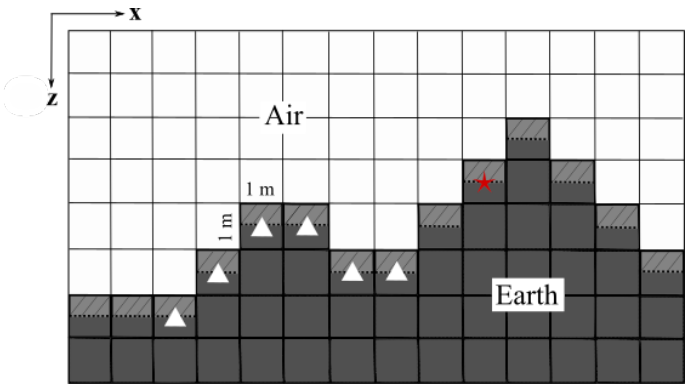

Figure 4.5: Topography on the standard staggered grid. Red star: source point; white triangles: receivers. Note the staircases that appear due to quantization of the elevation values.

Three sources located on different sides of the anticline structure were modeled, corresponding to Vibroseis sources only. The vertical-force point sources were placed inside the model at $(x_{214}, z_{214}) = (137\,\text{m}, 1340\,\text{m})$, $(x_{226}, z_{226}) = (3360\,\text{m}, 115\,\text{m})$, and $(x_{545}, z_{545}) = (6070\,\text{m}, 190\,\text{m})$, where the index refers to the ID of the source x- and z-coordinates (figure 4.6).

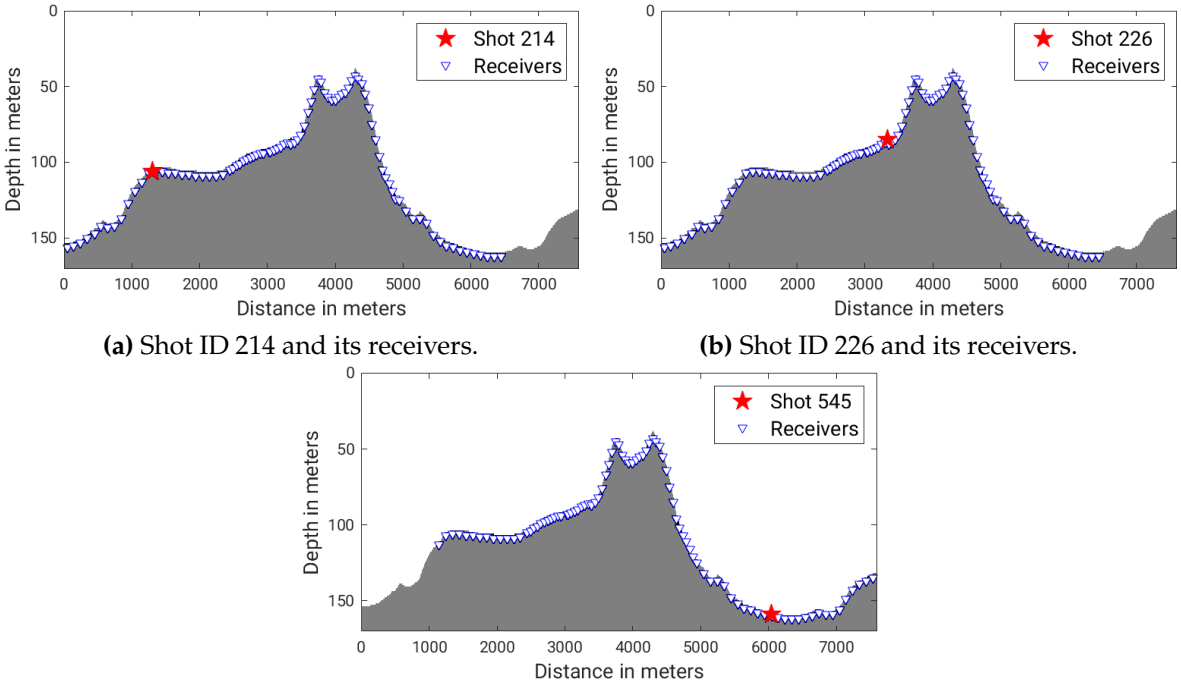

(a) Shot ID 214 and its receivers.

(b) Shot ID 226 and its receivers.

(c) Shot ID 545 and its receivers.

Figure 4.6: Positioning of shot point IDs 214, 226, and 545 and their corresponding receivers (vertical axis exaggerated).

4.2 Numerical tests

In order to ensure a stable simulation of the wavefield, a grid size test had to be conducted by comparing analytical and numerical criteria. The spatial grid spacing Δh was estimated using the grid dispersion criterion in equation 2.39. For a Taylor FD order of $n = 8$ in space,

a minimum velocity in the model of $v_{S_{min}} = 1097\,\mathrm{m/s}$ (taking anisotropy into account) and $f_{max} = 2\,f_c = 22\,\mathrm{Hz}$, I get a minimum wavelength of

$$\lambda_{min} = \frac{v_{Smin}}{f_{max}} \approx 50\,\mathrm{m}\ , \tag{4.2}$$

which leads to

$$\Delta h \leq \frac{\lambda_{min}}{n} \approx 6.2\,\mathrm{m}\ . \tag{4.3}$$

To avoid a violation of the Courant criterion, the time step size Δt is calculated according to equation 2.40. With the maximum velocity in the model of $v_{P_{max}} = 5290\,\mathrm{m/s}$ (again, taking anisotropy into account) and a second Taylor FD order in time, I get

$$\Delta t \leq \frac{\Delta h}{\beta\sqrt{2}\,v_{max}} \approx 0.83\,\mathrm{ms}\ , \tag{4.4}$$

with the factor β being the sum of the weighting coefficients of the FD Taylor operator (see subsection 2.2.3).

Based on these stability criteria, numerical tests were performed to confirm their validity and to ensure convergence of the modeled seismograms. For this purpose, different model discretizations were utilized as outlined in table 4.2. These tests have shown that there are no visible changes in first-arrival waveforms. Nevertheless, a grid spacing of $\Delta h = 1.0\,\mathrm{m}$ was finally chosen to avoid numerical artifacts, also known as the "staircase effect" (Moczo, Robertsson, et al., 2007).

Table 4.2: Discretization for numerical tests.

Δh in meters	Δt in milliseconds
6	0.6
4	0.4
3	0.3
2	0.2
1	0.1

Chapter 5

Results

As mentioned in section 2.1.3, anisotropy manifests itself in a directional dependence of the stress-strain relation and, therefore, of the wave velocity, i.e., for the P-wave velocity with a maximum for horizontal propagation and for the S-wave velocity with a maximum for directions of about 45° in the case of VTI media. Attenuation influences seismic wave propagation, too, dissipating its actual energy (section 2.1.2). In order to confirm both phenomena, I investigate the effect of anisotropy and attenuation on the first breaks using the vertical component of the particle velocity field only.

Note that the synthetic data are examined only with respect to their onset times, not with respect to their waveforms. As the geometrical spreading of a point source is different from the geometrical spreading of a line source with respect to amplitude, a 3D to 2D data transformation of the data would be required (Forbriger et al., 2014) for a proper amplitude comparison. However, I am not applying any type of correction as the focus of my work is to look primarily at the arrival times.

5.1 Anisotropy effects

5.1.1 Field data fit

In order to compare the synthetic data with the field data, I first filter the field data using a filter that passes the frequencies between 2 Hz and 20 Hz in different octave panels, with attenuation of 20 dB to 40 dB per octave below and above these frequencies, respectively. In the following, only a pure qualitative analysis will be presented.

Figure 5.1 shows the comparison of the field data with the isotropic and anisotropic synthetic shot gathers for the shot ID 214 (another representative shot is presented in the appendix - see figure D.2). Due to strong lateral and vertical changes of the geological structure, complex events can be observed in the synthetic gathers, from direct, reflected, and head waves to dominant surface waves. In the isotropic case, there is a good match between the first-arrival waveforms for the shallow depths and small offsets; a better match occurs with VTI modeled data especially at medium offsets around the energy-focusing effect; at both medium and larger offsets, the TTI modeling results show the best fit.

5.1.2 Trace comparison

The influence of anisotropy can be assessed by analyzing shot gathers individually. As reference, the elastic isotropic modeling is shown; figure 5.2a depicts the reference gather for shot ID 214. As previously mentioned, the surface waves clearly dominate the seismograms. As a consequence, I designed a window (figure 5.2b) to separate the first breaks from the other types of seismic events; at small offsets, near the source, I completely mute the traces.

Figures 5.2c and 5.2d depict a comparison between elastic isotropic and elastic VTI and TTI modeling, respectively. As expected, based on equation 2.28b, the direct waves in anisotropic simulations propagate faster than in isotropic simulations, as P-wave velocities increase; the shift in arrival time is, however, offset-dependent, i.e., larger time shifts at distant receivers. Taking into account that primarily far offsets are of interest for this study, in figure 5.3 I show a windowed single trace from an offset of 4150 m for a better comparison (see the little rectangles in figures 5.2c and 5.2d). A clear earlier arrival time in the elastic VTI case compared to the TTI case can be observed; this is caused by the presence of the Thomsen parameter ε in the VTI simulation, while for the TTI simulation the dip θ has an additional influence. Not only the traveltimes are affected, but also the waveforms, varying especially in the elastic VTI case. The same behavior holds for other shots, too (see figure D.3 in the appendix).

5.1.3 Wavefield comparison

The impact of anisotropy can be best visually assessed on simulated wavefields. Figure 5.4 depicts the simulated shot ID 214 wavefield in both isotropic and VTI cases (the TTI modeling result is not presented here as visually there are only minor wavefield changes compared to the VTI modeling result). As the subsurface model is heterogeneous and structures are steeply dipping, with waves propagating with different velocities in all directions, the wavefronts have very complex shapes and paths. In the VTI case, the wavefronts travel faster, a phenomenon that is well observed at the Keuper-Muschelkalk interface, where a significant amplitude change occurs due to the high velocity contrast; see the appendix (figure D.1) for another shot comparison.

By comparing wavefield snapshots of different modeled sources at later times, another important feature emerges: the wavefield penetration depth and the illumination of the salt body. In figure 5.5a, the wavefield snapshot of modeled shot IDs 214, 226, and 545 are depicted at $t \approx 2$ s. As shown in figure 4.6, the two sources are located at totally different locations: shot IDs 214 and 545 SW and NE of the main hill structure, respectively, and shot ID 226 very close to the peak of the hill, above the salt body. The seismic waves reach the reflectors along the salt flanks at large angles (compared to the normal to the reflectors), leading to potentially total reflection; almost all of the "energy" is then trapped in the upper layers of Cretaceous, Jurassic, and Keuper and almost none penetrates the salt body. In contrast, both modeled shot IDs 214 and 545 are able to penetrate the salt; a lot of the energy is also concentrated on top of the hill (strong topography effect), and head waves form in the layers above Buntsandstein, which makes it possible to image the upper part of the salt dome up to ca. 1000 m.

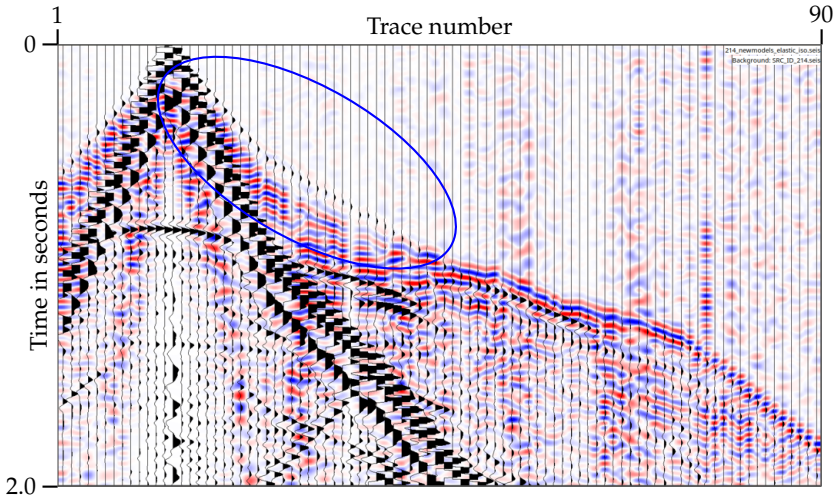

(a) Field data comparison with isotropic synthetic data.

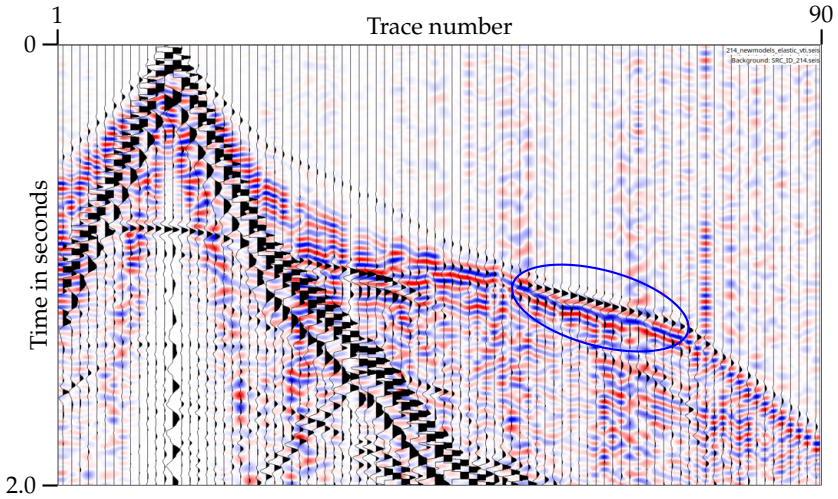

(b) Field data comparison with VTI synthetic data.

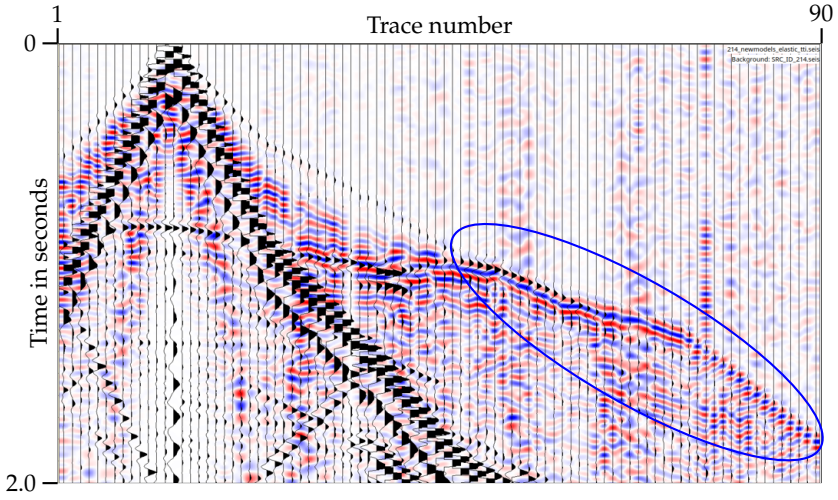

(c) Field data comparison with TTI synthetic data.

Figure 5.1: Shot ID 214: data fit between the field data (in the background in red and blue) and the synthetic data (in the foreground, represented by wiggles), both trace normalized; the first trace corresponds to offset 5230 m and the last trace to offset −1370 m. Multiple events can be observed, with an energy-focusing effect present at medium offsets. Blue-marked areas show a better fit with the field data.

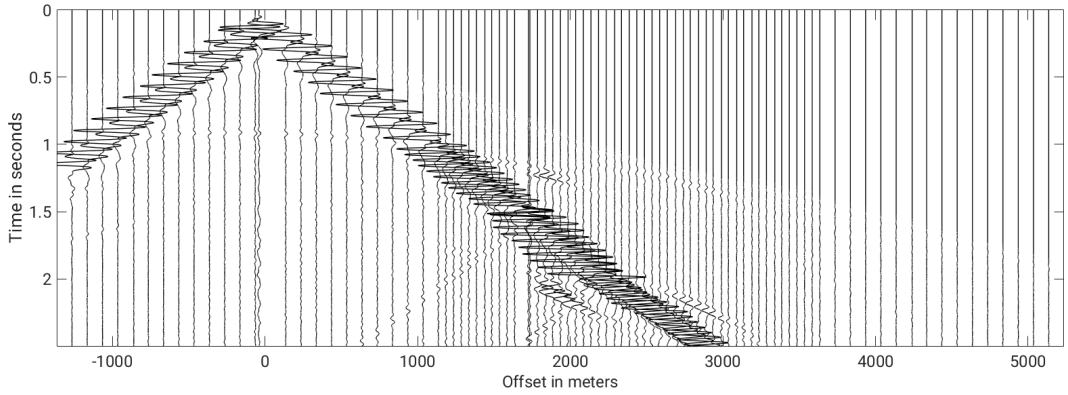

(a) Shot ID 214: elastic isotropic shot gather.

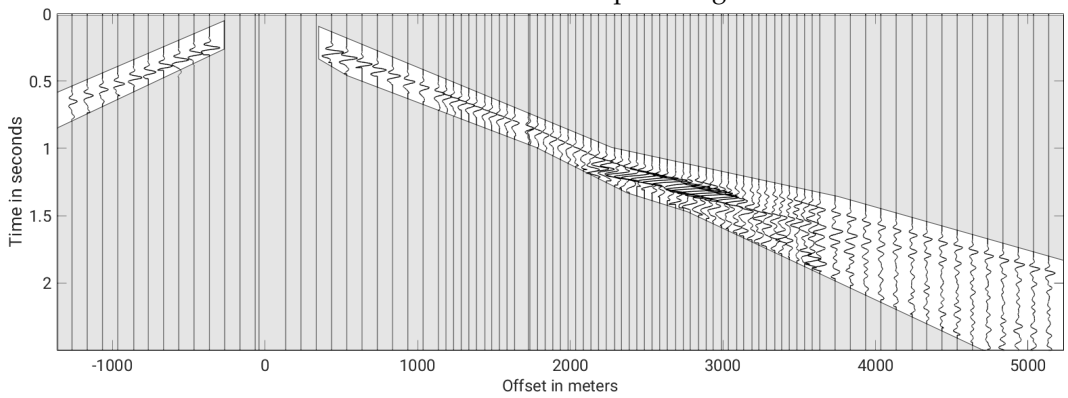

(b) Shot ID 214: elastic isotropic shot gather. The mute area is displayed in gray.

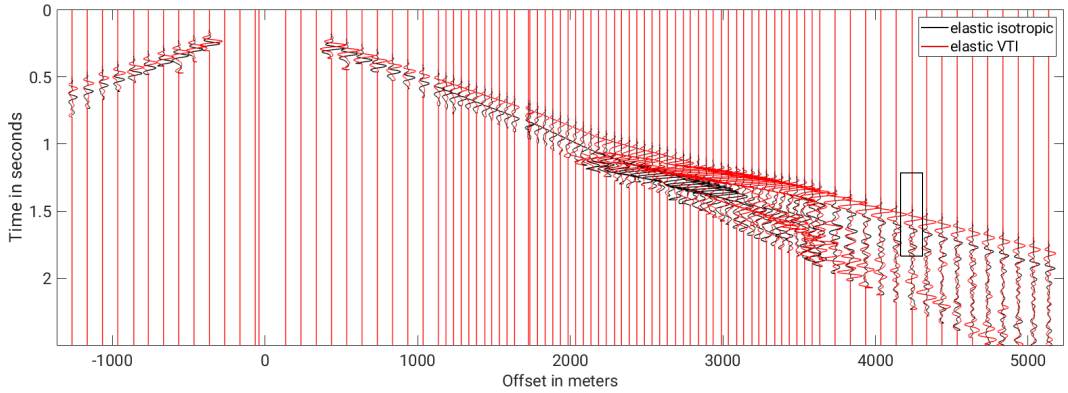

(c) Shot ID 214: elastic isotropic vs. elastic VTI shot gathers (windowed).

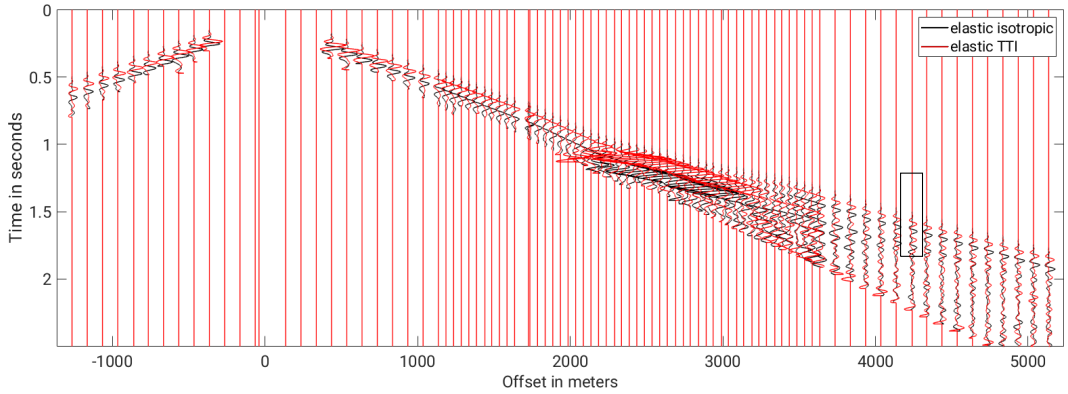

(d) Shot ID 214: elastic isotropic vs. elastic TTI shot gathers (windowed).

Figure 5.2: Shot ID 214: comparison of shot gathers. The first-arrival window corresponding to trace 80 is indicated by the black rectangle.

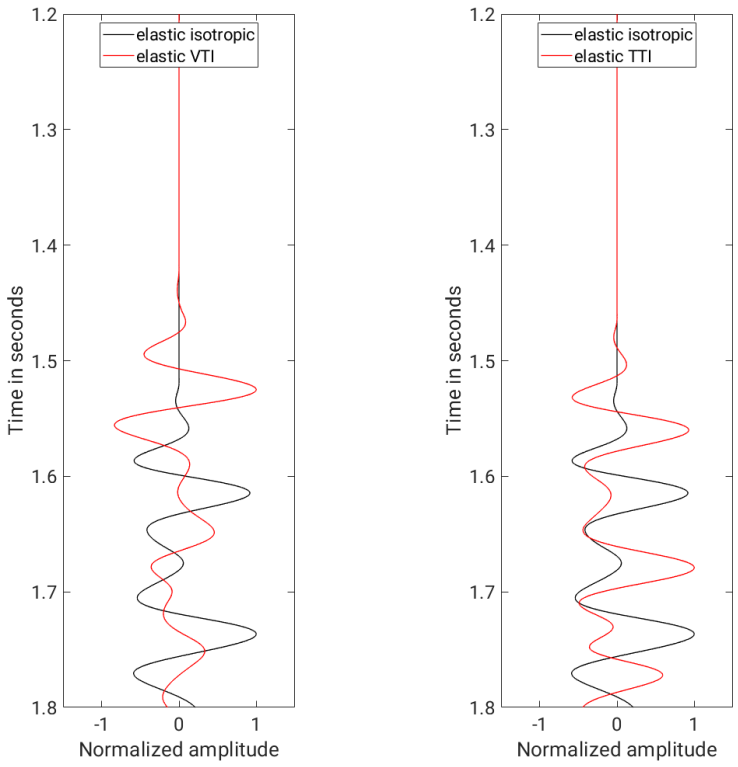

(a) Elastic isotropic vs. VTI. **(b)** Elastic isotropic vs. TTI.

Figure 5.3: Comparison of trace 80 for source ID 214, elastic isotropic vs. anisotropic modeling.

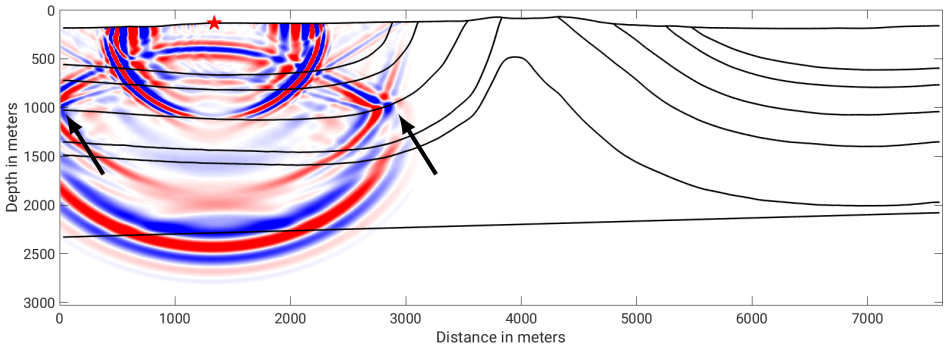

(a) Shot ID 214: isotropic wavefield.

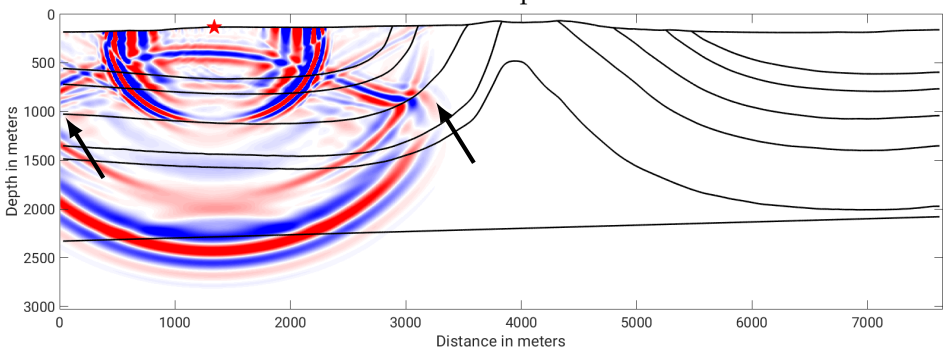

(b) Shot ID 214: VTI wavefield.

Figure 5.4: Shot ID 214: vertical particle velocity wavefield snapshots recorded at the same time ($t \approx 0.8\,\mathrm{s}$) with geological interfaces overlaid; each snapshot is individually normalized. No legend for the red-blue wavefield colors is shown as the values are clipped for a better visualization. Significant differences in the wavefields are marked with black arrows; the source position is marked with a red star.

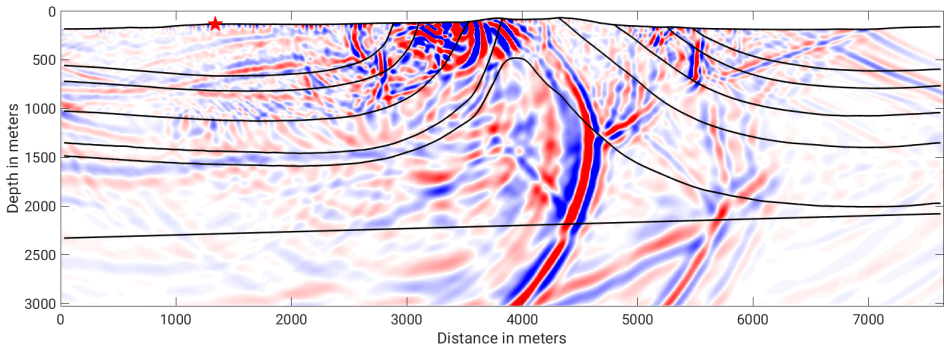

(a) Shot ID 214: VTI wavefield.

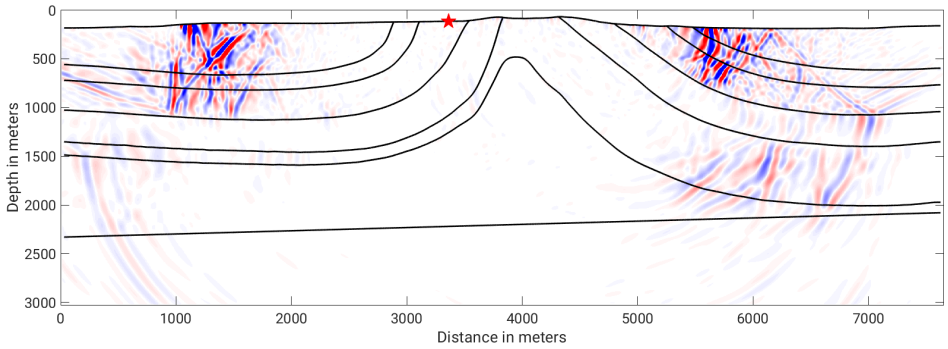

(b) Shot ID 226: VTI wavefield.

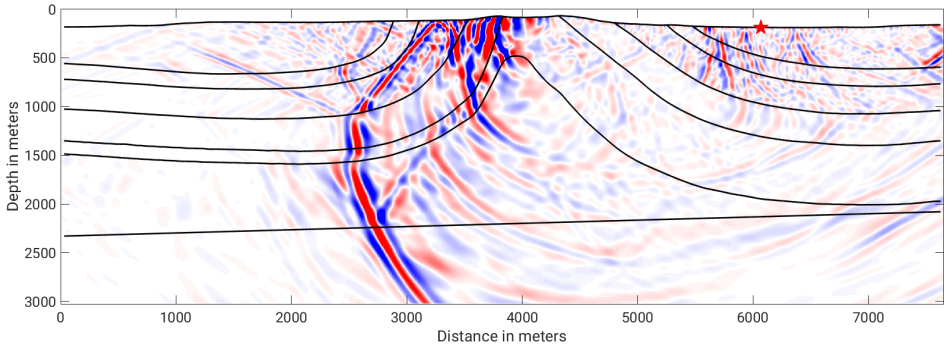

(c) Shot ID 545: VTI wavefield.

Figure 5.5: Shot IDs 214, 226, and 545: vertical particle velocity wavefield snapshots recorded at the same time ($t \approx 2\,\mathrm{s}$) with geological interfaces overlaid; each snapshots is individually normalized. No legend for the red-blue wavefield colors is shown as the values are clipped for a better visualization. The source position is marked with a red star. For shot ID 226, the seismic waves reach the reflectors along the salt flanks at large angles (compared to the normal to the reflectors) and total reflection occurs, leading to most of the "energy" trapped in the upper sedimentary layers and almost none of it penetrating the salt body; in contrast, shot IDs 214 and 545, located further away from the main salt body, penetrate the salt, even though a high percent of the "energy" is still concentrated on top of the hill; head waves form in the Keuper, Muschelkalk, and Buntsandstein layers, which means that the upper part of the salt dome can be illuminated up to ca. 1000 m depth.

5.2 Attenuation effects

The influence of attenuation can be assessed by analyzing modeled shot gathers individually. As reference, the elastic isotropic and VTI modeling are shown. Figure 5.6 depicts a comparison between elastic and viscoelastic isotropic modeling and elastic and viscoelastic VTI modeling, respectively. As expected, due to the high values of the quality factor Q and also due to the low frequencies, the attenuation effects are small, slightly increasing for far offsets. Due to the slight changes in waveforms between the elastic and viscoelastic modeling results, no field data fit or wavefield snapshots with viscoelasticity are shown.

Again, trace number 80, corresponding to offset 4150 m, is shown in figure 5.7. In comparison to the elastic modeling, in both viscoelastic isotropic and viscoelastic anisotropic modeling, a slightly earlier arrival time for the first arrivals appears, with no visible waveform change. The anisotropic modeling outlines the faster-propagating and changed waveforms that occur when the Thomsen parameters are considered (subfigure 5.7c). The same behavior holds for other shots, too (see figure D.4 in the appendix).

Conclusions from the tests and results just presented will be given in the next chapter.

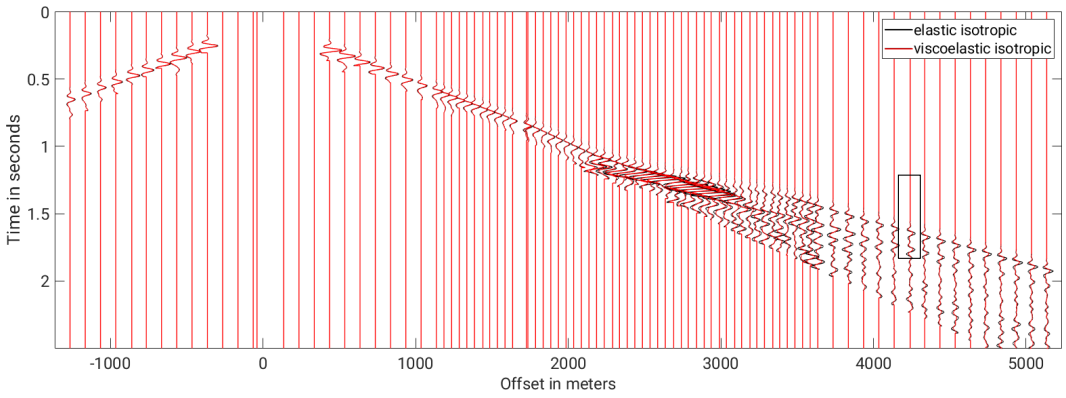

(a) Shot ID 214: elastic vs. viscoelastic isotropic (windowed).

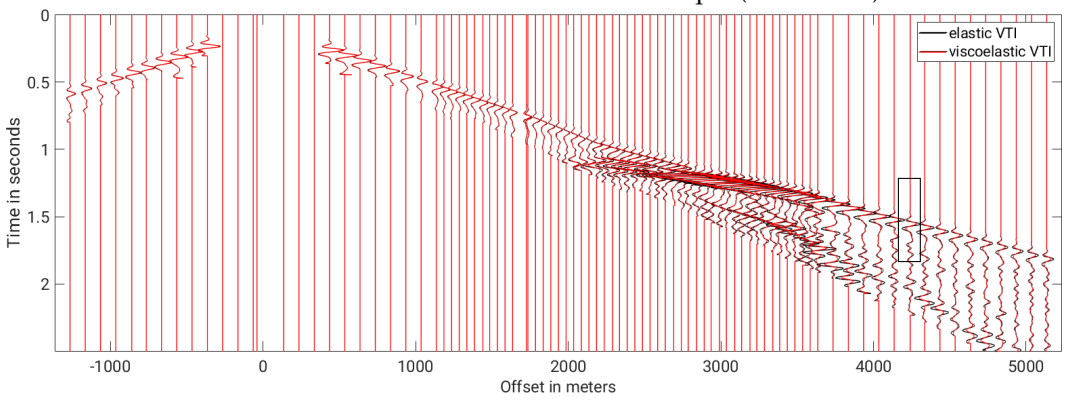

(b) Shot ID 214: elastic vs. viscoelastic VTI (windowed).

Figure 5.6: Shot ID 214: comparison of shot gathers. This is, again, muted data; the same window as in figure 5.2b was used. The first-arrival window corresponding to trace 80 is indicated by the black rectangle.

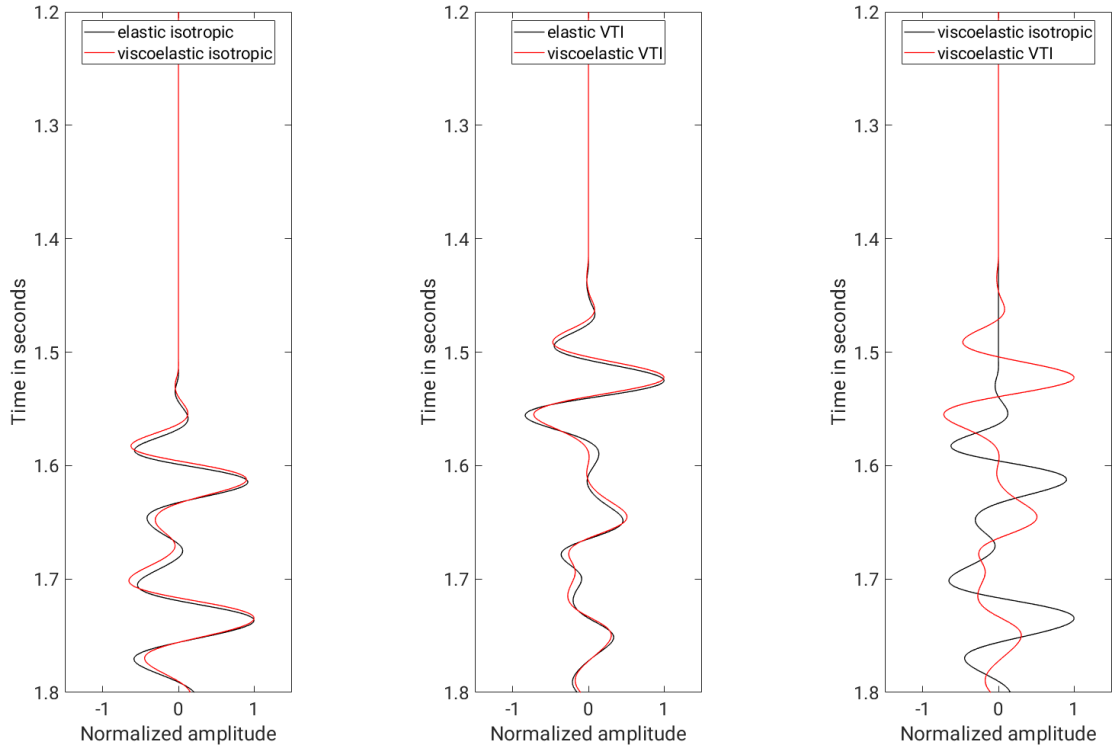

(a) Isotropic comparison. **(b)** VTI comparison. **(c)** Viscoelastic comparison.

Figure 5.7: Comparison of trace 80 for source ID 214, elastic isotropic vs. viscoelastic isotropic, elastic VTI vs. viscoelastic VTI, and viscoelastic isotropic vs. viscoelastic VTI modeling, respectively.

Chapter 6

Conclusions and outlook

The present work analyzed the elastic and viscoelastic anisotropic wave propagation at the Asse II nuclear waste repository to check on the possibility of applying full-waveform inversion (FWI) at low frequencies up to 20 Hz in the future. For this purpose, a 2D finite-difference (FD) vertical-transverse isotropy (VTI) and tilted-transverse isotropy (TTI) forward solver for P- and SV-waves was implemented. The main objectives were (a) the investigation of the quality of the simplified parameter models to see if they already meet the prerequisites for FWI and (b) the analysis of how anisotropy and attenuation influence the onset times of the first breaks.

The parameter models were determined from previously known geological structures and recently acquired 3D seismic field data over the Asse-Heeseberg hill. These data are meant to improve the detail of the available subsurface information, in particular the boundaries of the salt body, the structures in the overburden, the fault systems, and the possible fluid migration paths. Given the complex geology, with horizontal layering, the presence of a salt dome with steep flanks, and the change of stress conditions, is was expected that transverse isotropy needs to be considered. Weak transverse isotropy can be described by the so-called Thomsen parameters ε and δ. While VTI considers a vertical symmetry axis, TTI needs another parameter, namely the tilt angle θ of the symmetry axis, which can also vary spatially and follow geological structures.

The forward simulations show that anisotropy has a significant impact on the seismic wavefield, as the velocities perpendicular and parallel to the symmetry axis differ. In a close comparison of isotropic and VTI modeling, first breaks occur earlier when anisotropy is considered; the effect of anisotropy is offset-dependent, as far offsets involve longer and more horizontal wave propagation paths. The difference between VTI and TTI modeling is present but minor; the tilt angle, which varies quite significantly in the subsurface, complicates the effects of anisotropy. It is clear, though, that in this context ignoring anisotropy definitely leads to wrong seismic interpretations. Considering that the Asse salt structure is geologically complex and steeply dipping, TTI modeling is the preferred way to correctly map the subsurface in high resolution and match the first-arrival traveltimes, especially at long offsets.

Wavefield modeling results show that good illumination up to depths of ca. 1000 m (including the upper part of the salt dome) can be achieved. Yet, this only holds for shots located further away from the hill, as shots located directly above the salt structure are not able to illuminate the salt flanks significantly, since the dipping reflectors are hit at large angles, leading to total reflection. In general, due to the presence of the high-velocity contrast at the Keuper-Muschelkalk interface, most of the seismic "energy" is trapped in the sedimentary layers above, which makes imaging any structures below rather complicated.

Given the existence of attenuative layers in the study area, considering viscoelasticity would seem the most appropriate way to approximate the subsurface. However, the tests have shown that the effects of attenuation are negligible at frequencies below 20 Hz, given the relatively large Q values here. Nevertheless, different results would be expected if higher frequencies and more relaxation parameters were considered. Even though this would lead to a better structural imaging with representative amplitudes, it would also require more computational resources.

All in all, I can say that the objectives of this thesis were achieved and that certain conclusions can be drawn for a potential FWI application on first-arrival waveforms at low frequencies. The results demonstrate that, in general, the physical parameter models are sufficient and valid for FWI, as they explain many features present in the field data acquired over the Asse hill, at least at longer offsets. Structural imaging using near offsets, however, may require a refined near-surface model. While it is essential to incorporate anisotropy, attenuation represents only a minor factor. In other words, the most realistic scenario would be the application of viscoelastic TTI modeling. Yet, due to memory and CPU requirements, for practical reasons it is recommended to use elastic TTI modeling in low-frequency FWI.

Bibliography

Bai, T. (2019). "Modeling, imaging and waveform inversion in attenuative anisotropic media". PhD thesis. Colorado School of Mines, p. 127.

Bai, T. and Tsvankin, I. (2016). "Time-domain finite-difference modeling for attenuative anisotropic media". *Geophysics* 81.2, pp. C69–C77. DOI: 10.1190/GEO2015-0424.1.

Bai, T., Tsvankin, I., and Wu, X. (2017). "Waveform inversion for attenuation estimation in anisotropic media". *Geophysics* 82.4, WA83–WA93. DOI: 10.1190/GEO2016-0596.1.

Blanch, J., Robertsson, J., and Symes, W. (1995). "Modeling of a constant Q: Methodology and algorithm for an efficient and optimally inexpensive viscoelastic technique." *Geophysics* 60, pp. 176–184. DOI: 10.1190/1.1443744.

Bohlen, T. (2002). "Parallel 3-D viscoelastic finite difference seismic modelling". *Computers and Geosciences* 28.8, pp. 887–899. DOI: 10.1016/S0098-3004(02)00006-7.

Bohlen, T., De Nil, D., Köhn, D., and Jetschny, S. (2016). *SOFI2D - seismic modeling with finite differences. 2D - elastic and viscoelastic version (updated 2022)*. Karlsruhe Institute of Technology. URL: https://git.scc.kit.edu/GPIAG-Software/SOFI2D.

Bond, W. L. (1943). "The Mathematics of the Physical Properties of Crystals". *Bell System Technical Journal* 22.1, pp. 1–72. DOI: 10.1002/j.1538-7305.1943.tb01304.x.

Bundesamt für Strahlenschutz (2017). *Asse: 3D seismic measurements*. URL: https://archiv.bge.de/archiv/www.asse.bund.de/Asse/EN/topics/what-will-become/seismic-measurements/seismicmeasurements_node.html (visited on 06/30/2022).

Bundesanstalt für Geowissenschaften und Rohstoffe (2021). *Asse II mine*. URL: https://www.deutsche-rohstoffagentur.de/DE/Themen/Endlagerung/Standorte/Asse/asse_node.html (visited on 06/30/2022).

Bundesgesellschaft für Endlagerung (2015). *Rückholung der radioaktive Abfälle aus der Schachtanlage Asse II - Konzeptplanung für die Rückholung der radioaktive Abfälle von der 725- und 750-m-Sohle*. Tech. rep., p. 145.

Bundesgesellschaft für Endlagerung (2018). *Bericht zur Revisionskartierung (M 1:5.000) der Salzstruktur Asse im Bereich zwischen Groß Denkte und Klein Vahlberg*. Tech. rep., p. 93.

Bundesgesellschaft für Endlagerung (2020). *3D-Seismic Asse: Bearbeitung und Interpretation*. Tech. rep.

Bundesgesellschaft für Endlagerung (2021). *Einblicke #8: das Magazin der Bundesgesellschaft für Endlagerung*. Tech. rep. URL: https://www.einblicke.de/magazine/einblicke-8/.

Bundesgesellschaft für Endlagerung (2022). *Asse: 3D seismic survey*. URL: https://www.bge.de/de/asse/themenschwerpunkte/themenschwerpunkt-3d-seismik/ (visited on 06/30/2022).

Carcione, J. M., Kosloff, D., and Kosloff, R. (1988). "Wave-propagation simulation in an elastic anisotropic (transversely isotropic) solid". *The Quarterly Journal of Mechanics and Applied Mathematics* 41.3, pp. 319–346. DOI: 10.1093/qjmam/41.3.319.

Carcione, J. M. (2007). *Wave fields in real media: Wave propagation in anisotropic, anelastic, porous and electromagnetic media*. Vol. 38. Elsevier.

Center for Wave Phenomena, Colorado School of Mines (2022). *Seismic Unix*.

Courant, R., Friedrichs, K., and Lewy, H. (1928). "Über die partiellen Differenzengleichungen der mathematischen Physik. Mathematische Annalen". *Geophysics* 100.1, pp. 32–74. DOI: 10.1007/BF01448839.

Crase, E., Pica, A., Noble, M., McDonald, J., and Tarantola, A. (1990). "Robust elastic nonlinear waveform inversion: Application to real data". *Geophysics* 55, pp. 527–538. DOI: 10.1190/1.1442864.

Falk, J. (1998). "Efficient seismic modeling of small-scale inhomogeneities by the finite-difference method". PhD thesis. University of Hamburg.

Forbriger, T., Groos, L., and Schäfer, M. (2014). "Line-source simulation for shallow-seismic data. Part 1: theoretical background". *Geophysical Journal International* 198.3, pp. 1387–1404. DOI: 10.1093/gji/ggu199.

Gardner, G. H. F., Gardner, L. W., and Gregory, A. R. (1974). "Formation velocity and density — The diagnostic basics for stratigraphic traps". *Geophysics* 39.6, pp. 770–780. DOI: 10.1190/1.1440465.

Gauthier, O., Virieux, J., and Tarantola, A. (1986). "Two-dimensional nonlinear inversion of seismic waveforms: numerical results". *Geophysics* 51.7, pp. 1387–1403. DOI: 10.1190/1.1442188.

Hammersley, J. and Lees-Miller, J. (2022). *Overleaf*. URL: https://www.overleaf.com/edu/kit.

Hupe, T., Orlowsky, D., and Draganov, D. (2022). "Passive Seismic Interferometry as a Tool for Seismic Imaging from Mine Galleries". *Conference Proceedings, 83rd EAGE Annual Conference & Exhibition* 2022, pp. 1–5. DOI: 10.3997/2214-4609.202210168.

Hupe, T., Orlowsky, D., Swoboda, U., and M., S. (2020). "Combination of 3D Borehole Radar and Underground Reflection Seismic - A Case Study for In-Mine Exploration". *NSG2020 3rd Conference on Geophysics for Mineral Exploration and Mining* 2020, pp. 1–5. DOI: 10.3997/2214-4609.202020031.

Knopoff, L. and McDonald, G. (1958). "Attenuation of small amplitude stress waves in solids". *Reviews of Modern Physics* 30, pp. 1178–1192.

Komatitsch, D., Barnes, C., and Tromp, J. (2000). "Simulation of anisotropic wave propagation based upon a spectral element method". *Geophysics* 65.4, pp. 1251–1260. DOI: 10.1190/1.1444816.

Komatitsch, D. and Martin, R. (2007). "An unsplit convolutional Perfectly Matched Layer improved at grazing incidence for the seismic wave equation". *Geophysics* 72. DOI: 10.1190/1.2757586.

Komatitsch, D. and Martin, R. (2009). "An unsplit convolutional perfectly matched layer technique improved at grazing incidence for the viscoelastic wave equation". *Geophysical Journal International* 179.1, pp. 333–344. DOI: 10.1111/j.1365-246X.2009.04278.x.

Komatitsch, D. and Tromp, J. (1999). "Introduction to the spectral element method for three-dimensional seismic wave propagation". *Geophysical Journal International* 139.3, pp. 806–822. DOI: 10.1046/j.1365-246x.1999.00967.x.

Levander, A. (1988). "Fourth-order finite-difference P-SV seismograms". *Geophysics* 53, pp. 1425–1436. DOI: 10.1190/1.1442422.

Liu, H.-P., Anderson, D. L., and Kanamori, H. (1976). "Velocity dispersion due to anelasticity; implications for seismology and mantle composition". *Geophysical Journal of the Royal Astronomical Society* 47.1, pp. 41–58. DOI: 10.1111/j.1365-246X.1976.tb01261.x.

MATLAB (2021). *Version R2021a*. Natick, Massachusetts: The MathWorks Inc.

Moczo, P., Kristek, J., Vavrycuk, V., Archuleta, R., and Halada, L. (2002). "Heterogeneous staggered-grid finite-difference modeling of seismic motion with volume harmonic and arithmetic averaging of elastic moduli and densities". *Bulletin of the Seismological Society of America* 92, pp. 3042–3066.

Moczo, P., Robertsson, J., and Eisner, L. (2007). "The finite-difference time-domain method for modeling of seismic wave propagation". *Advances in Geophysics* 48, pp. 421–516.

O'Connell, R. J. and Budiansky, B. (1978). "Measures of dissipation in viscoelastic media". *Geophysical Research Letters* 5, pp. 5–8. DOI: 10.1029/GL005i001p00005.

Oh, J. W., Shin, Y., Alkhalifah, T., and Min, D. J. (2020). "Multistage elastic full-waveform inversion for tilted transverse isotropic media". *Geophysical Journal International* 223.1, pp. 57–76. DOI: 10.1093/gji/ggaa295.

Pollok, L., Saßnowski, M., Kühnlenz, T., Gundelach, V., Hammer, J., and Pritzkow, C. (2018). "Geological exploration and 3D model of the Asse salt structure for SE expansion of the Asse II mine". *Mechanical Behaviour of Salt IX, 2018 Proceedings*, pp. 753–763.

Rafavich, F., Kendall, C. S. C., and Todd, T. (1984). "The relationship between acoustic properties and the petrographic character of carbonate rocks". *Geophysics* 49.10, pp. 1622–1636.

Robertsson, J., Blanch, J. O., and Symes, W. (1994). "Viscoelastic finite-difference modeling". *Geophysics* 59, pp. 1444–1456. DOI: 10.1190/1.1443701.

Saßnowski, M., Pollok, L., Kuehnlenz, T., Hammer, J., and Pritzkow, C. (2018). "Detailed petrographic and structural studies of salt rocks as basis for an internal geological 3D-model of the Asse salt structure (German Zechstein)". *Mechanical Behavior of Salt IX, 2018 Proceedings*, pp. 765–774.

Shearwater GeoServices Software, Inc. (2022). *Shearwater Reveal*.

Szymaniak, T. and Schäfer, M. (2002). "Geologisch-tektonische Kartierung der Salzstruktur Asse im Subhercynen Becken". PhD thesis. Technische Universität Clausthal, p. 97.

Tarantola, A. (1984). "Inversion of seismic reflection data in the acoustic approximation". *Geophysics* 49.8, pp. 1259–1266. DOI: 10.1190/1.1441754.

TGS (2017). *Anisotropic Parameter Estimation*. URL: https://www.tgs.com/products-services/processing/imaging/depth-technologies/iso-vti-tti-ort-tort (visited on 07/12/2022).

Thomsen, L. (1986). "Weak elastic anisotropy". *Geophysics* 51.10, pp. 1954–1966. DOI: 10.1190/1.1442051.

Trela, J., Massaka, V., Potepa, P., Bilgili, F., Gärtner, G., and Teichmann, L. (2021). "Quantum nodal system-Asse 3D survey success story". *First Break* 39.1, pp. 61–68. DOI: 10.3997/1365-2397.fb2021003.

Tsvankin, I. (2012). *Seismic Signatures and Analysis of Reflection Data in Anisotropic Media, Third Edition*. Society of Exploration Geophysicists. DOI: 10.1190/1.9781560803003.

Virieux, J. (1986). "P-SV wave propagation in heterogeneous media: velocity-stress finite difference method". *Geophysics* 51, pp. 889–901. DOI: 10.1190/1.1442147.

Voigt, W. (1910). *Lehrbuch der Kristallphysik*. Leipzig, Berlin: B. G. Teubner.

Wikipedia (2010). *Asse hill*. URL: https://commons.wikimedia.org/wiki/File:Asse_bei_Wolfenb%C3%BCttel.jpg (visited on 07/12/2022).

Zahradnik, J., Moczo, P., and Hron, F. (1993). "Testing four elastic finite difference schemes for behaviour at discontinuities". *Bulletin of the Seismological Society of America* 83, pp. 107–129. DOI: 10.1785/BSSA0830010107.

Zellmer, H. and Holländer, R. (1996). *Stratigraphisches Profil der Umgebung von Braunschweig*. Tech. rep. Braunschweig: Inst. f. Geowissenschaften der TU Braunschweig, p. 1.

Zener, C. M. (1948). *Elasticity and Anelasticity of Metals*. Vol. 55. University of Chicago Press, Chicago Illinois, p. 170.

Zhu, Y. and Tsvankin, I. (2006). "Plane-wave propagation in attenuative transversely isotropic media". *Geophysics* 71.2, pp. 17–30. DOI: 10.1190/1.2187792.

List of Figures

List of Tables

Acknowledgments

First of all, I would like to thank Prof. Dr. Thomas Bohlen not only for involving me in this project, but also for his guidance and all the discussions we had during the last few years. I would also like to address many thanks to the entire BGE team for their remarkable cooperation during this project phase, especially to Maximilian Scholze. Many thanks also go to Prof. Dr. Stefan Buske from TU Bergakademie Freiberg for accepting to be the second reviewer of my thesis.

Next, I would like to express all my gratitude for the whole Applied Geophysics work group. First, to Thomas Hertweck and Lars Houpt for always being there, helping with technical problems, proofreading my thesis and all everyday discussions, ice creams, and (planned) table tennis matches we had together. Then, to the students from our institute for the pleasant working environment and all lunch breaks and meet-ups we had. Many thanks also go to Claudia Payne and Ellen Gottschämmer for all their help and support during the past three years.

Last, but not least, I would like to thank my mother for her infinite love and, of course, for being the perfect role model for what a woman can represent in the field of Geosciences. Then, to Edward and his family for being the support I need, and to all my amazing friends.

Appendix A

Software

I take this opportunity to acknowledge the software I have used in the present work:

- MATLAB, with an academic license (MATLAB, 2021): general data display, pre-processing, snapshot visualization, and seismogram processing;
- Reveal, with an academic license (Shearwater GeoServices Software, Inc., 2022): seismic data visualization;
- Seismic Unix (Center for Wave Phenomena, Colorado School of Mines, 2022): seismic processing;
- SOFI2D (Bohlen et al., 2016): 2D finite-difference forward modeling;
- Overleaf, with a Professional KIT campus license (Hammersley and Lees-Miller, 2022): writing and editing.

Appendix B

Geology and stratigraphy

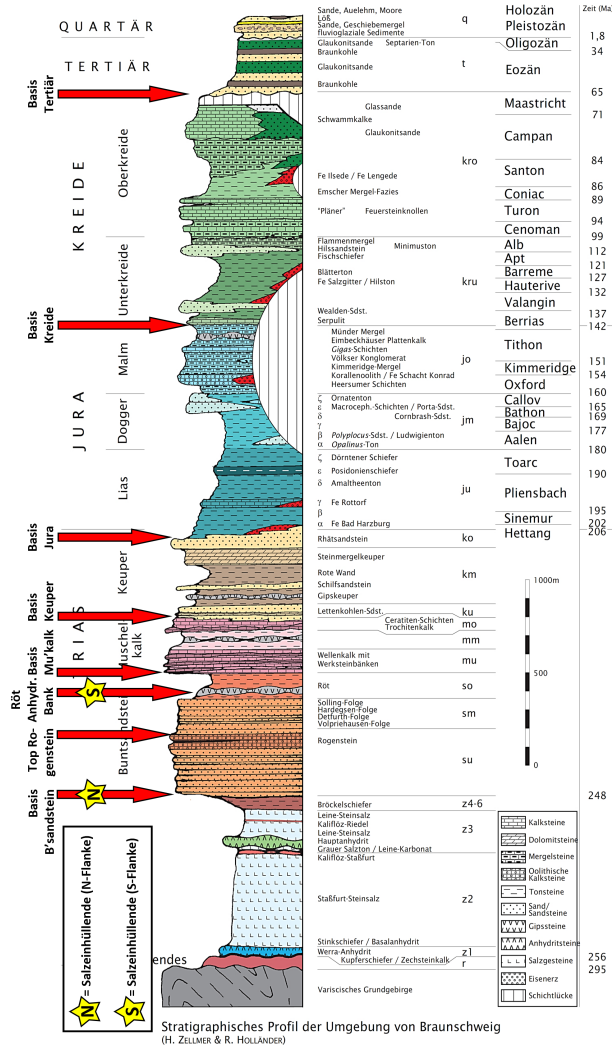

Figure B.1: Stratigraphic profile of the area around Braunschweig (modified after Zellmer and Holländer, 1996 and Bundesgesellschaft für Endlagerung, 2021).

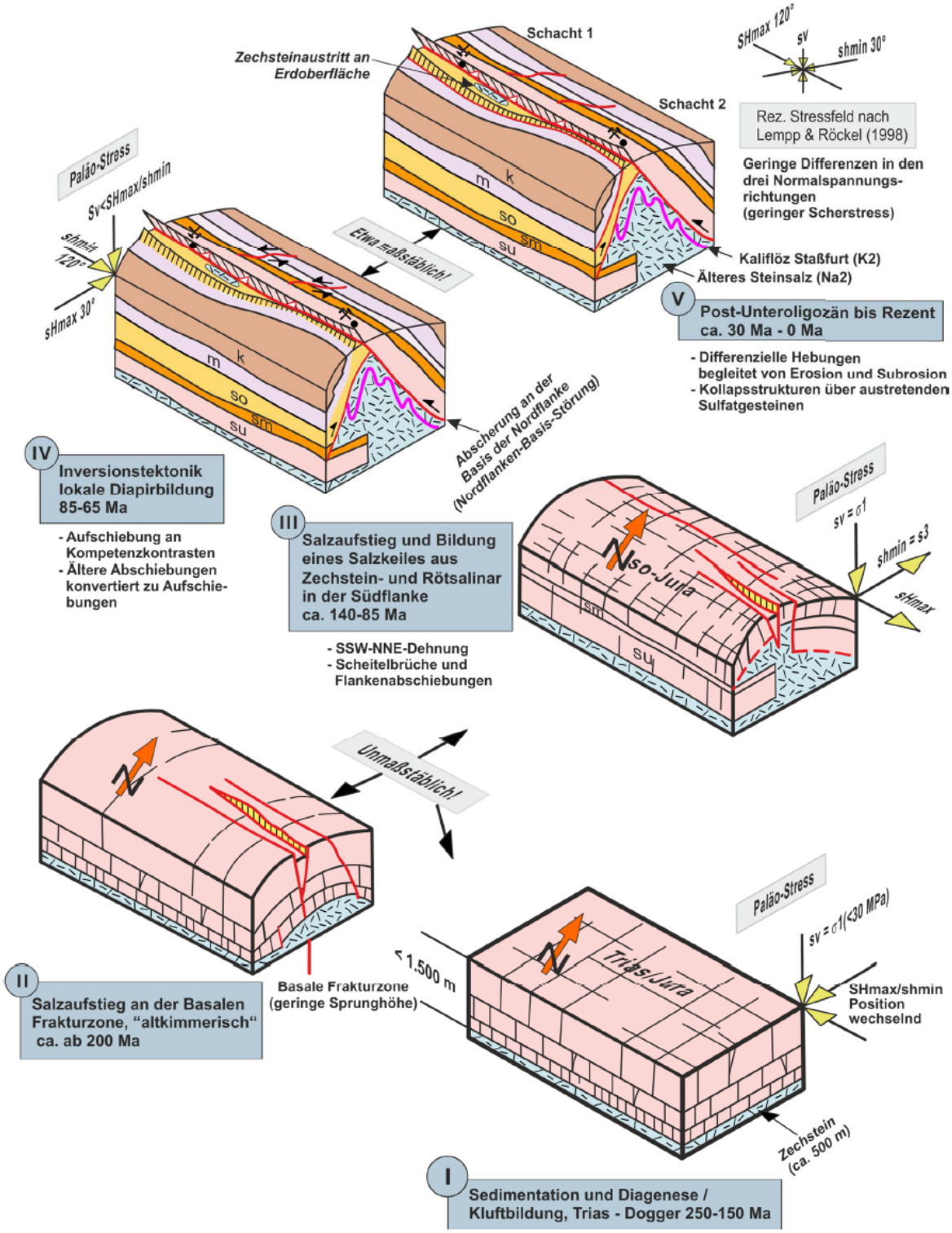

Figure B.2: Schematic sketch of the tectonic history of the Asse salt formation (Bundesgesellschaft für Endlagerung, 2018).

Appendix C

Overview maps

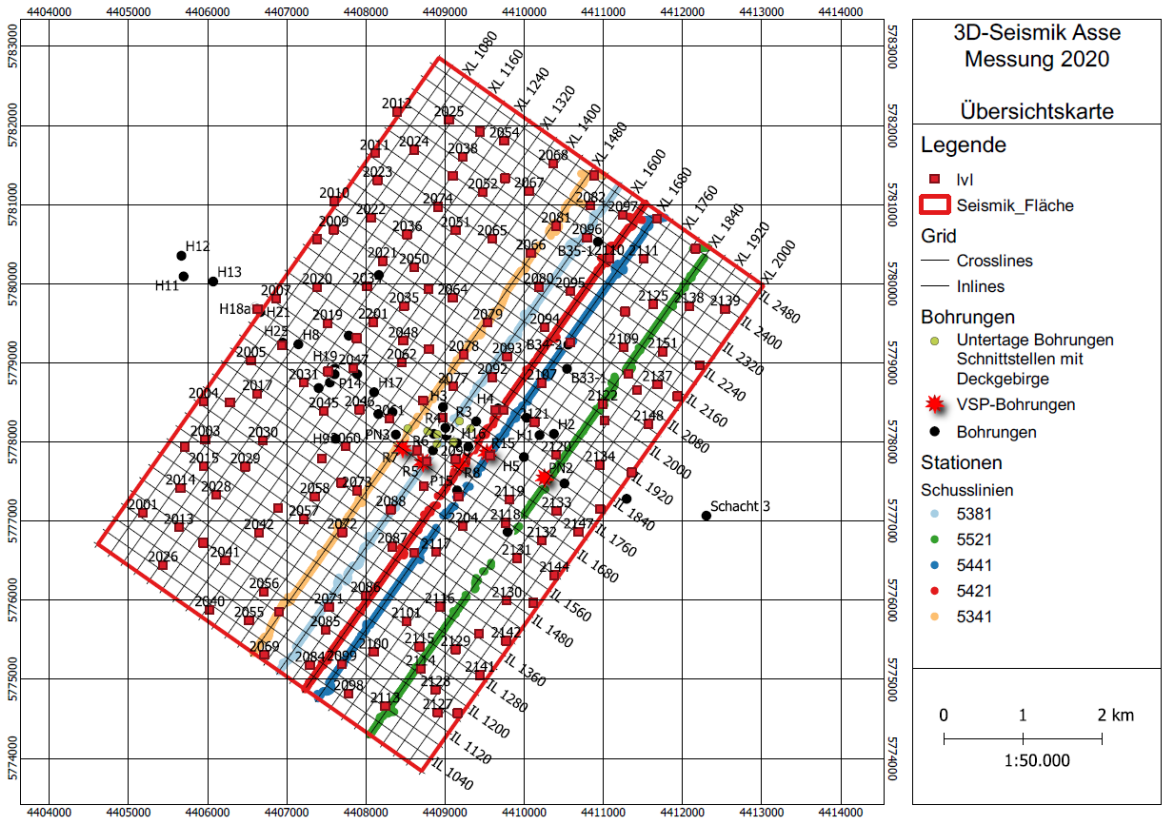

Figure C.1: 3D seismic survey: wells, vertical-seismic-profiling (VSP) and low-velocity-layer (lvl) surveys. Source line 5421 (here in red) corresponds to the analyzed crossline 1641 (Bundesgesellschaft für Endlagerung, 2020).

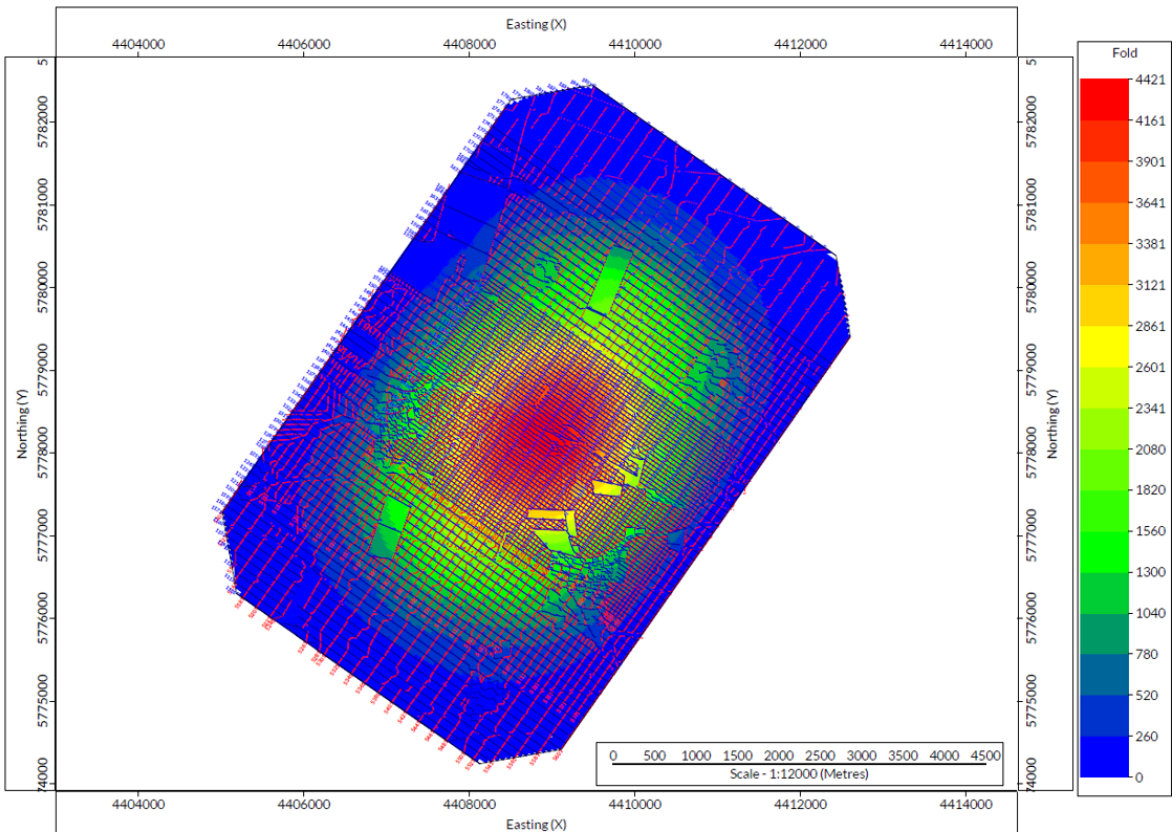

Figure C.2: Common-midpoint (CMP) fold map (Bundesgesellschaft für Endlagerung, 2020).

Appendix D

Seismograms and wavefields

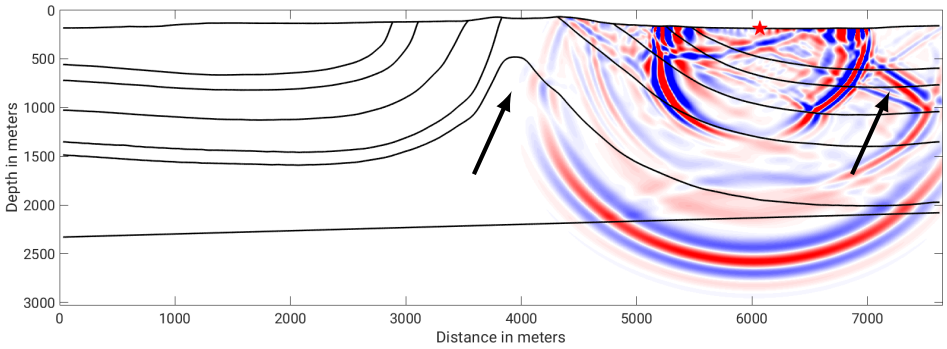

(a) Shot ID 545: isotropic wavefield.

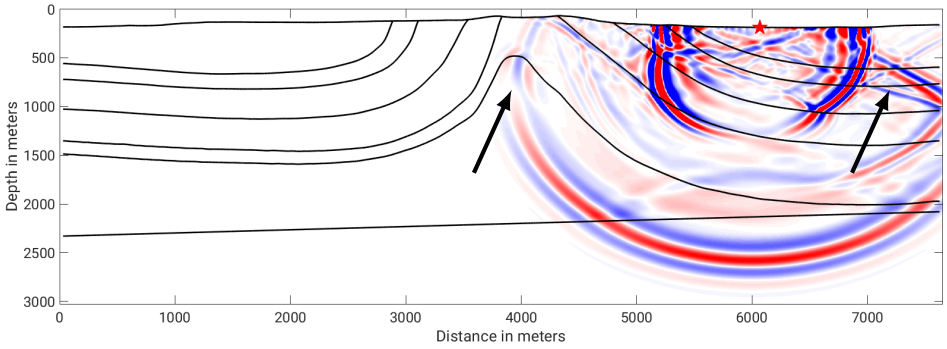

(b) Shot ID 545: VTI wavefield.

Figure D.1: Shot ID 545: vertical particle velocity wavefield snapshots recorded at the same time ($t \approx 2\,\mathrm{s}$) with geological interfaces overlaid; each snapshot is individually normalized. No legend for the red-blue wavefield colors is shown as the values are clipped for a better visualization. Significant differences in wavefield are marked with black arrows; the source position is marked with red.

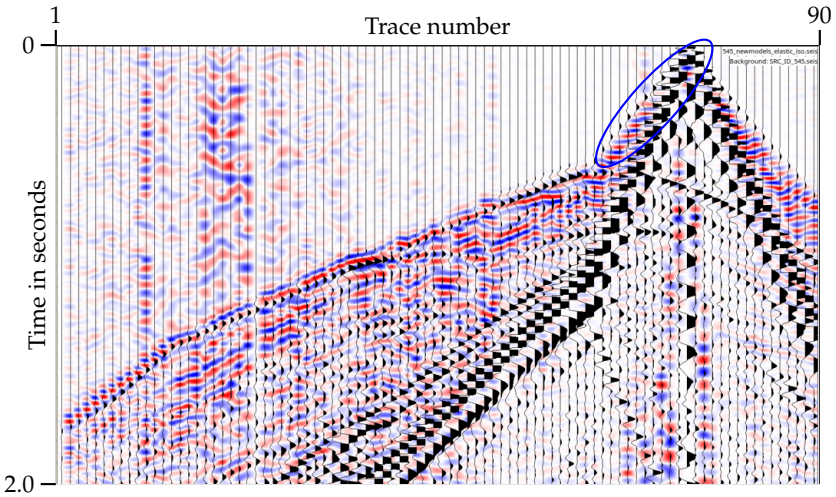

(a) Field data comparison with isotropic synthetic data.

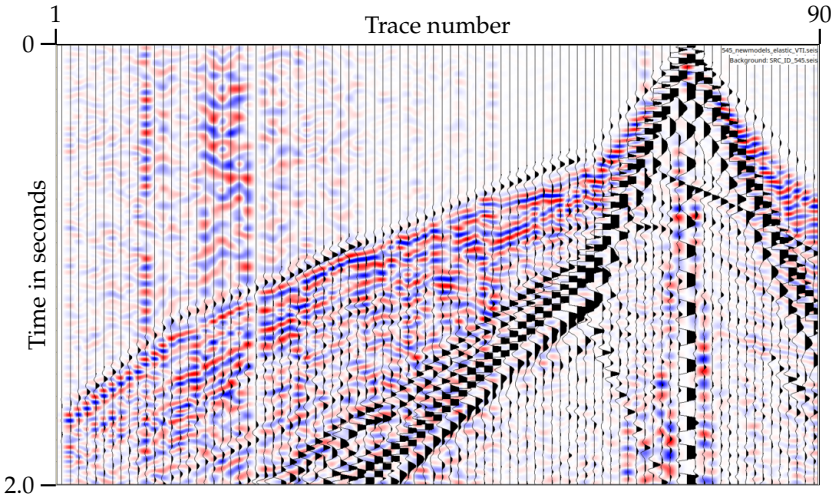

(b) Field data comparison with VTI synthetic data.

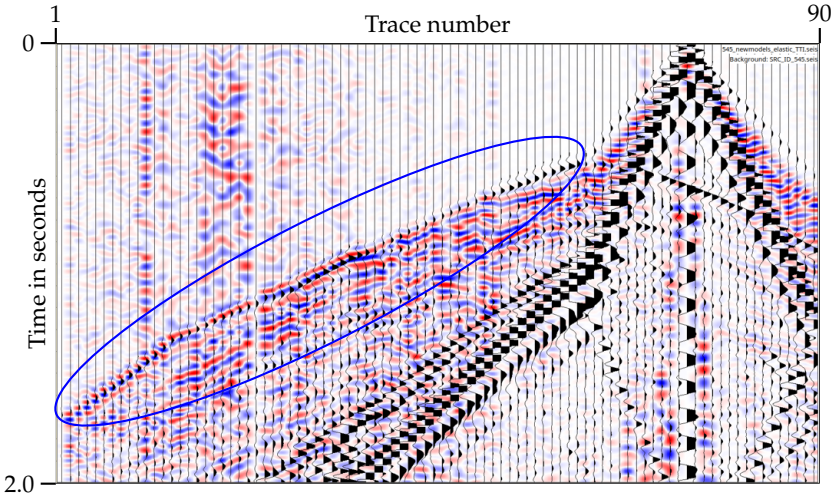

(c) Field data comparison with TTI synthetic data.

Figure D.2: Shot ID 545: data fit between the field data (in the background in red and blue) and the synthetic data (in the foreground, represented by wiggles), both trace normalized; the first trace corresponds to offset −4950 m and the last trace to offset 1500 m Multiple events can be observed. Blue-marked areas show a better fit with the field data.

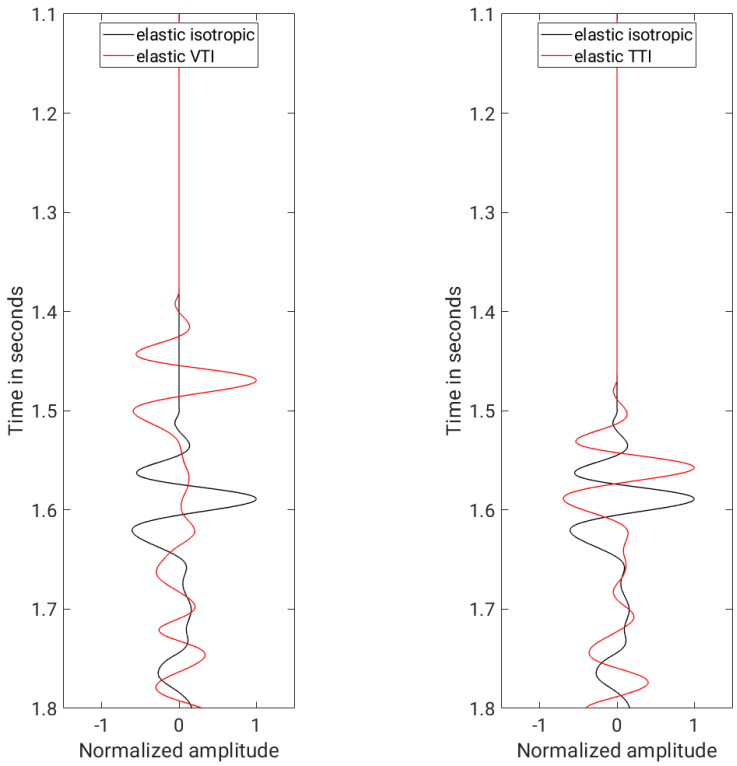

(a) Elastic isotropic vs. VTI. **(b)** Elastic isotropic vs. TTI.

Figure D.3: Comparison of trace 10 for source ID 545, elastic isotropic vs. anisotropic modeling.

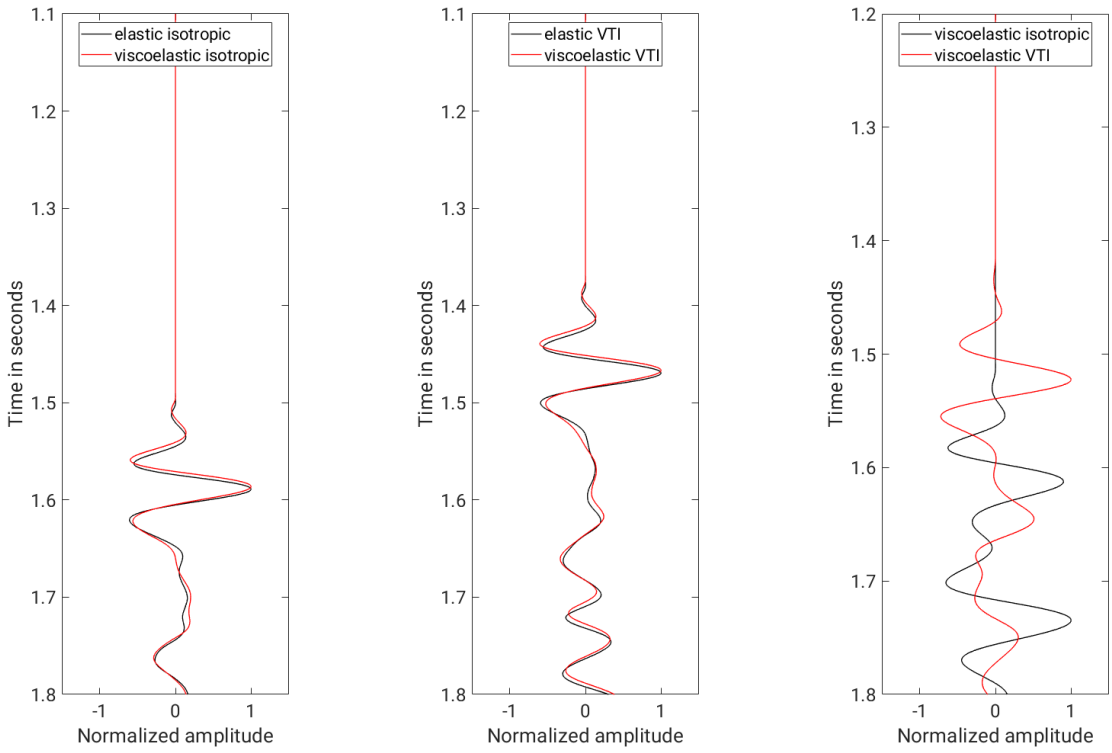

(a) Isotropic comparison. **(b)** VTI comparison. **(c)** Viscoelastic comparison.

Figure D.4: Comparison of trace 10 for source ID 545, elastic isotropic vs. viscoelastic isotropic, elastic VTI vs. viscoelastic VTI, and viscoelastic isotropic vs. viscoelastic VTI modeling, respectively.